UNIVERSITY OF LEEDS

This is a repository copy of *Analysis of the shearing instability in nonlinear convection and magnetoconvection*.

White Rose Research Online URL for this paper:
http://eprints.whiterose.ac.uk/982/

eprints@whiterose.ac.uk
https://eprints.whiterose.ac.uk/

Citation for the published paper
Rucklidge, A.M. and Matthews, P.C. (1996) *Analysis of the shearing instability in nonlinear convection and magnetoconvection.* Nonlinearity, 9 (2). pp. 311-351.

Citation for this paper
To refer to the repository paper, the following format may be used:

Rucklidge, A.M. and Matthews, P.C. (1996) *Analysis of the shearing instability in nonlinear convection and magnetoconvection.* Author manuscript available at: http://eprints.whiterose.ac.uk/archive/00000982/ [Accessed: *date*].

Published in final edited form as:

Rucklidge, A.M. and Matthews, P.C. (1996) *Analysis of the shearing instability in nonlinear convection and magnetoconvection.* Nonlinearity, 9 (2). pp. 311-351.

Analysis of the shearing instability in nonlinear convection and magnetoconvection

A M Rucklidge and P C Matthews§

Department of Applied Mathematics and Theoretical Physics,
University of Cambridge, Cambridge CB3 9EW, UK

Abstract. Numerical experiments on two-dimensional convection with or without a vertical magnetic field reveal a bewildering variety of periodic and aperiodic oscillations. Steady rolls can develop a shearing instability, in which rolls turning over in one direction grow at the expense of rolls turning over in the other, resulting in a net shear across the layer. As the temperature difference across the fluid is increased, two-dimensional pulsating waves occur, in which the direction of shear alternates. We analyse the nonlinear dynamics of this behaviour by first constructing appropriate low-order sets of ordinary differential equations, which show the same behaviour, and then analysing the global bifurcations that lead to these oscillations by constructing one-dimensional return maps. We compare the behaviour of the partial differential equations, the models and the maps in systematic two-parameter studies of both the magnetic and the non-magnetic cases, emphasising how the symmetries of periodic solutions change as a result of global bifurcations. Much of the interesting behaviour is associated with a discontinuous change in the leading direction of a fixed point at a global bifurcation; this change occurs when the magnetic field is introduced.

1. Introduction

Over the past thirty years or more, the shearing instability of convection rolls has been discovered and rediscovered many times. Most studies have focused either on the linear behaviour at the onset of the instability, or on the highly supercritical behaviour in the turbulent regime. In contrast, we examine mildly nonlinear behaviour, using a combination of truncated ordinary differential equation (ODE) models and one-dimensional maps to explain the spatio-temporal transitions that we observe in the partial differential equations (PDEs) for two-dimensional (2D) convection. In particular, we examine the role of global bifurcations in determining whether or not the direction of the shear changes over the course of unsteady behaviour. An example of such a reversing oscillation, known as a pulsating wave (PW) is shown in Figure 1.

Convection in a horizontal layer heated from below typically begins with a cellular pattern (for example, rolls, squares or hexagons). Rolls, which are separated by vertical planes of mirror symmetry, may become unstable to a mode that breaks this mirror symmetry and generates a net shear across the layer. The physical mechanism behind this instability is well understood: suppose a pair of rolls initially with vertical

§ Present address: Department of Theoretical Mechanics, University of Nottingham, Nottingham NG7 2RD, UK
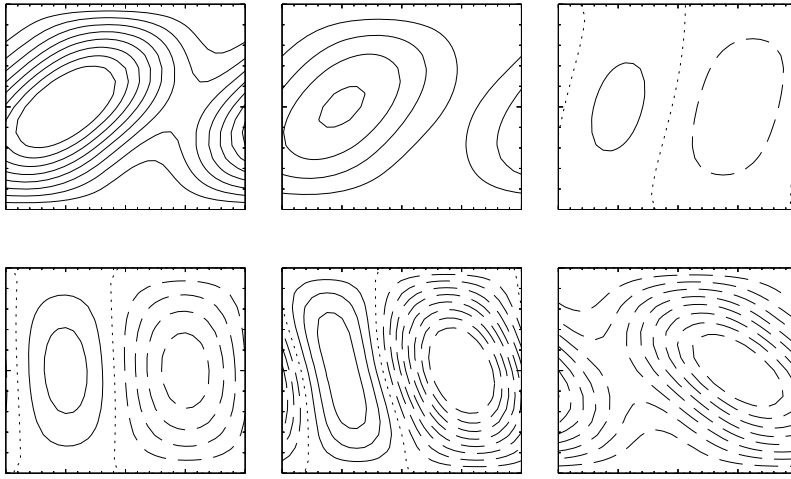
Figure 1. A pulsating wave (PW) in convection in a vertical magnetic field (from Matthews *et al* 1993, with permission). The spacing between the streamlines is uniform and is the same in each frame. The zero streamline is dotted and negative streamlines are dashed. The parameters (defined in sections 2 and 3) are $\sigma = 0.5$, $\zeta = 0.2$, $L = 0.378$, $Q = 63.2$ ($q = 0.10$) and $R = 10\,687$ ($r = 1.50$). The pulsating wave is shown at times $t = 0, 0.08, 0.14, 0.26, 0.41, 0.50P$, where P is the period of the oscillation: after half a period, the direction of the streaming has reversed and the system is in a state that is the mirror image of its initial condition.

rising and descending plumes tilts over, say to the right. The rising plume, now moving up and to the right, will transport rightward momentum to the top of the layer, while the descending plume will transport leftward momentum to the bottom of the layer. This results in a horizontal streaming motion with a net shear across the layer, which may be enough to sustain the original tilt of the rolls. Moreover, the shear enhances the clockwise roll and suppresses the anti-clockwise roll. The instability is favoured if the rolls are narrow because of the greater effect that tilting has on narrow rolls. In a finite box, the shear will drive a mean circulation on the scale of the width of the box, while the convective rolls act on the scale of the depth of the box. This mechanism, in which parallel vortices can drive a flow on a scale larger than the vortices themselves, is independent of the force that drives the vortices (buoyancy in this case), and so is relevant to a variety of fluid mechanical problems, as illustrated in an experiment by Tabeling *et al* (1990).

Large-scale mean flows are observed in a variety of astrophysical and geophysical contexts, and this shearing mechanism has been put forward as a way of driving these flows. An example of a shear flow being driven by the transport of momentum by tilted convection is the differential rotation of the Sun (Rüdiger 1989). A similar process may drive the zonal flows of Jupiter (Busse 1983) and Venus (Thompson 1970). Matthews *et al* (1992) considered the onset of convection in an imposed oblique magnetic field as a model of penumbral convection in a sunspot, and discovered mean flows driven by tilted rolls. Drake *et al* (1992) invoked this instability to explain shearing flows in the edge of Tokamak plasmas, where vortices are driven by the curved magnetic boundary. The instability may be responsible for the breakup of narrow salt fingers

in double-diffusive convection (Proctor & Hughes 1991).

Large-scale flows and tilted rolls have been observed in laboratory experiments on convection. Willis & Deardorff (1970) reported rolls that oscillated between tilting to the left and tilting to the right. Krishnamurti & Howard (1981) observed large-scale circulation in turbulent convection in an annulus, in one direction at the top and in the other at the bottom. The presence of mean flows in this and other experiments on turbulent convection has been reviewed by Siggia (1994).

The full symmetry of convection in a 2D periodic box is $O(2)$: the system is invariant under translations and reflections in a vertical plane. Rolls near the onset of convection break the translational symmetry but are invariant under reflections in the vertical plane that separates them. Such rolls will be referred to as steady symmetric (SS) convection. There is a continuous family of rolls generated by the broken translation symmetry $SO(2)$. The residual mirror symmetry may be broken in a pitchfork bifurcation, leading to a steady shear across the layer and one roll growing at the expense of the other (Proctor & Weiss 1993). In a stratified fluid, the dominance of one roll over the other means that the tilted rolls will travel steadily.

However, in an incompressible fluid (modelled using the Boussinesq approximation) with the same boundary conditions at the top and bottom, the equations have an additional symmetry: reflection in the horizontal mid-plane, which implies that SS rolls have point symmetry about their centres. In this case, the vertical mirror symmetry can be broken in two distinct types of pitchfork bifurcation. First, the mirror symmetry can be broken while the point symmetry of the original rolls is preserved. Any motion in one direction at the top will be balanced by an equal and opposite motion at the bottom, so breaking the mirror symmetry will not lead to travelling rolls but to steady tilted convection (STC). Second, both the mirror symmetry and the point symmetry can be broken (but their product preserved), which leads to travelling rolls. We concentrate on the Boussinesq case in this paper and examine only point-symmetric solutions with spatial periodicity imposed (as in, for example, Figure 1). In doing so, we fix the phase of the rolls in the periodic box, and only two of the continuous family of SS rolls persist: those with clockwise rolls and those with anti-clockwise rolls in the right half of the box. The continuous translation symmetry now reduces to discrete translations through half the period of the original rolls, which interchange clockwise and anti-clockwise rolls. The product of this discrete translation symmetry with the original mirror symmetry results in a second mirror symmetry in the vertical plane that bisects one of the rolls, again interchanging clockwise and anti-clockwise rolls. Thus there are two mirror symmetries important in our problem and the spatial symmetry group is D_2, the symmetry group of a rectangle. The reflections are both in vertical planes: reflection in the plane that separates SS rolls and leaves them unchanged, and reflection in the plane that bisects one of the rolls and changes the direction of their circulation. The first is important in compressible and incompressible convection, and the second is important in incompressible convection with imposed point symmetry, the case that we consider. We discuss the relevance of our results to convection in a compressible layer in the final section.

The mirror symmetry that leaves SS rolls invariant may also be broken in a Hopf bifurcation (Landsberg & Knobloch 1991; Proctor & Weiss 1993), which leads to oscillations in which the direction of the shear alternates. In the compressible case, rolls will travel first in one direction and then back again as the direction in which the dominant rolls are tilted changes; there is no net drift of the pattern over the whole oscillation. These oscillations have a spatio-temporal symmetry: they are invariant

under the advance of half a period in time followed by a reflection in a vertical plane (compare the first and last frames of Figure 1), and have been termed direction-reversing travelling waves (DRTW) by Landsberg & Knobloch (1991), pulsating waves (PW) by Proctor & Weiss (1993) and sloshing oscillations by Lantz (1995) in different contexts. In the Boussinesq case, the Hopf bifurcation, like the pitchfork bifurcation, can break the mirror symmetry in two distinct ways, either preserving or breaking the point symmetry of the rolls. We use the term pulsating wave to describe a point-symmetric oscillation, in which the rolls do not travel (as in Figure 1), and direction-reversing travelling wave to describe an oscillation in which the rolls break the point symmetry and do travel back and forth. Prat *et al* (1995) have found Hopf bifurcations to both PW and DRTW in the PDEs for 2D Boussinesq convection with no-slip boundary conditions, indicating that the shearing instability is not an artifact of the stress-free boundary conditions that we use. As we are imposing point symmetry, we exclude the possibility of DRTW in this paper.

Pulsating waves have been observed numerically in a number of two- and three-dimensional incompressible and compressible convective systems, with and without a magnetic field, and with a variety of boundary conditions. They can arise in a Hopf bifurcation from SS rolls, as described above, but they can also be created in a global bifurcation (Rucklidge & Matthews 1993; Matthews *et al* 1993; Proctor *et al* 1994). The pitchfork from SS to STC can be followed by a secondary Hopf bifurcation to oscillatory tilted convection (OTC), in which the magnitude of the shear varies but the direction does not change. As parameters are varied, this OTC periodic orbit grows and may (along with its mirror image) collide with the SS roll solution, glue together in a global bifurcation, and create a PW periodic orbit. In this gluing bifurcation, there is a gain of symmetry: the PW oscillations have a spatio-temporal symmetry that OTC lack. In this paper, we explore the different types of global bifurcations that arise in different parameter regimes, with and without a magnetic field, in order to study the symmetries of the different types of periodic orbits that appear and to elucidate the mechanisms that cause the direction of the shear to reverse.

In order to study these global bifurcations in detail, we construct truncations of the PDEs, in which the amplitudes of the most important modes are governed by a low-order set of ODEs. One advantage of this method is that the amount of computation required is greatly reduced, allowing a much more thorough investigation of parameter space than would be possible by solving the PDEs. Others have pursued this approach to understanding the shearing instability. The first to do so were Howard & Krishnamurti (1986), who truncated the non-magnetic Boussinesq PDEs in the spirit of Lorenz (1963), and found a variety of global bifurcations and chaotic oscillations. Hermiz *et al* (1995) improved the Howard & Krishnamurti (1986) truncation by including an additional shearing mode. Brummell & Julien (1996) have extended the model to include modes that break the point symmetry. Lantz (1995) included a horizontal magnetic field and found PW created both in a Hopf bifurcation and in a gluing bifurcation from OTC. Here we consider the case of an imposed vertical magnetic field, in addition to clarifying the transitions that occur in non-magnetic convection.

Since it is the behaviour of the PDEs that we are aiming to explain, it is important to understand how faithfully the behaviour of a truncated set of ODEs represents that of the PDEs. Close to the onset of convection, the amplitudes will be small and the truncation will be reliable, so it is desirable to find a small parameter that brings all the interesting bifurcations close to the initial bifurcation to SS rolls. Hughes & Proctor

(1990) introduced the limit of narrow rolls in a model of salt fingers, and Proctor & Weiss (1990) and Rucklidge (1992; 1994) used the same limit to construct model ODEs that gave asymptotically correct solutions to sets of PDEs describing thermosolutal convection and magnetoconvection, close to the initial bifurcation. We use the same limit of narrow rolls and the limit of small Prandtl number, and although we have not demonstrated that the resulting model ODEs give asymptotically exact solutions of the PDEs, through a careful choice of parameter regimes, we will show that the ODE model is a useful guide to understanding the dynamics of the PDEs, particularly for narrow rolls and small σ (as amplitudes are small and Rayleigh numbers close to critical), and near global bifurcations. The reason that the model works well near global bifurcations is that the dynamics of a system near a global bifurcation is determined primarily by the symmetries of the system, by the connections between the fixed points and by the leading eigenvalues. (The leading eigenvalues are those that have real parts closest to zero.) Hence the dynamics of the ODE model and the PDEs will be similar as long as the connections between the fixed points are the same and the eigenvalues at those fixed points are ordered in the same way.

Local bifurcations in systems with symmetry are well understood and equivariant bifurcation theory successfully explains the many types of solutions that can occur (Golubitsky *et al* 1988; Crawford & Knobloch 1991). The theory of global bifurcations in systems with symmetry is not so well developed. Global bifurcations are often associated with increases of symmetry (as in the gluing bifurcation mentioned above), even if the dynamics is chaotic (Dellnitz & Heinrich 1995). In this paper, we show how a heteroclinic gluing bifurcation, which increases the symmetry of a periodic orbit when there is no magnetic field, can split (as soon as the magnetic field is non-zero) into a series of homoclinic and heteroclinic bifurcations some of which are associated with changing symmetry, rather than increasing or decreasing symmetry. This behaviour is associated with a discontinuous change in the leading stable direction at the heteroclinic bifurcation. We construct a one-dimensional map that captures the behaviour of the ODE model and the PDEs and carry out a two-parameter study of its behaviour. This work is an important step in unravelling the role of global bifurcations in the dynamics of systems with symmetry.

Convection in three dimensions, with the additional symmetry of exchanging the two horizontal directions, shows a more complicated form of the shearing instability in which the alignment of the convection rolls and the shear flow can alternate. Such alternating pulsating waves can arise in a Hopf bifurcation from square convection (Rucklidge 1996); numerical examples are given by Matthews *et al* (1995, 1996) and by Rucklidge & Matthews (1995). The analysis of the global bifurcations of shearing behaviour in three-dimensional (3D) convection will be considered in future papers. Here, we restrict our attention to two dimensions because a study of the 2D case is a necessary prelude to understanding the 3D problem, and because the bifurcation from 2D to 3D behaviour can take place at various points in the 2D scenario. In particular, all the 2D behaviour we describe in this paper can occur in 3D simulations (Matthews *et al* (1995) have found PW in the 3D PDEs), and even when the dynamics is fully three dimensional, the system may visit 2D subspaces and be influenced by the dynamics within those subspaces.

In section 2, we present the PDEs for 2D magnetoconvection and in section 3 derive low-order models that describe the shearing oscillation in the presence of a vertical magnetic field. The notation we use to identify fixed points, periodic orbits and bifurcations is given in section 4. We discuss the non-magnetic case in section 5

Table 1. Symmetries of magnetoconvection (after Proctor & Weiss 1993). These symmetries generate an eight-element group; the other elements are $m' = ml$, $t_m = mt_e$, $t_l = lt_e$ and $t_{m'} = m't_e$.

e:	$(x, z, t) \rightarrow (x, z, t)$	$(\Psi, \theta, A) \rightarrow (\Psi, \theta, A)$
m:	$(x, z, t) \rightarrow (-x, z, t)$	$(\Psi, \theta, A) \rightarrow (-\Psi, \theta, -A)$
l:	$(x, z, t) \rightarrow (L + x, z, t)$	$(\Psi, \theta, A) \rightarrow (\Psi, \theta, A)$
t_e:	$(x, z, t) \rightarrow (x, z, t + \frac{1}{2}P)$	$(\Psi, \theta, A) \rightarrow (\Psi, \theta, A)$

and the magnetic case in section 6, addressing the question of the reversal of the shear using the techniques of nonlinear dynamics, and comparing the predictions of the low-order models with solutions of the PDEs. We discuss the relevance of our work to other examples of the shearing instability in section 7.

2. PDEs for two-dimensional magnetoconvection

The PDEs for 2D Boussinesq convection in a vertical magnetic field are:

$$\frac{\partial \omega}{\partial t} + \mathrm{J}\left(\Psi, \omega\right) = \sigma \nabla^2 \omega - \sigma R \frac{\partial \theta}{\partial x} - \sigma \zeta Q \left(\frac{\partial \nabla^2 A}{\partial z} + \mathrm{J}\left(A, \nabla^2 A\right) \right), \quad (2.1)$$

$$\frac{\partial \theta}{\partial t} + \mathrm{J}\left(\Psi, \theta\right) = \nabla^2 \theta + \frac{\partial \Psi}{\partial x}, \quad (2.2)$$

$$\frac{\partial A}{\partial t} + \mathrm{J}\left(\Psi, A\right) = \zeta \nabla^2 A + \frac{\partial \Psi}{\partial z}, \quad (2.3)$$

where $\omega = -\nabla^2 \Psi$ is the vorticity, Ψ is the streamfunction, θ is the deviation from the conducting temperature profile, A is the deviation of the flux function from a uniform vertical magnetic field, and x, z and t are the horizontal, vertical and time coordinates respectively (Knobloch *et al* 1981). The nonlinearities in the equations are in the operator $\mathrm{J}(f, g) = (\partial f/\partial x)(\partial g/\partial z) - (\partial g/\partial x)(\partial f/\partial z)$. The physical parameters are the Prandtl number σ and magnetic diffusivity ratio ζ, the Rayleigh number R (proportional to the temperature difference across the layer) and the Chandrasekhar number Q (proportional to the square of the imposed magnetic field). The boundary conditions are chosen for mathematical convenience: $\Psi = \omega = \theta = \partial A/\partial z = 0$ on the top and bottom walls ($z = 0, 1$). We impose periodic horizontal boundary conditions in a box of length $2L$ and define k, the spatial wave number, by $k = \pi/L$. The equations have a trivial solution $\Psi = \omega = \theta = A = 0$.

We will be dealing with point-symmetric solutions, which do not drift, so we need consider only the discrete reflection symmetries. The symmetries relevant to this problem (using the notation of Proctor & Weiss 1993) are given in Table 1: these are the identity e, reflections m and m' in the vertical planes $x = 0$ and $x = \frac{1}{2}L$ and their product, the translation l by a distance L. The reflection m leaves the SS rolls unchanged. Since we will be considering time-periodic solutions with period P, we also require the symmetry t_e, the advance of half a period in time. Along with the products of these elements, they form the eight element group $D_2 \times Z_2$, with each element its own inverse. The time advance symmetry operation arises naturally when considering the effect of a spatial reflection on a periodic orbit (Golubitsky *et al* 1988), as there are three possible outcomes when operating on a periodic orbit with a reflection: either a

Table 2. Effect of the spatial symmetries on the mode amplitudes.

m:	$(\Psi_{11}, \theta_{02}, \Psi_{12}, \Psi_{01}, A_{01}) \to (\Psi_{11}, \theta_{02}, -\Psi_{12}, -\Psi_{01}, -A_{01})$
l:	$(\Psi_{11}, \theta_{02}, \Psi_{12}, \Psi_{01}, A_{01}) \to (-\Psi_{11}, \theta_{02}, -\Psi_{12}, \Psi_{01}, A_{01})$
m':	$(\Psi_{11}, \theta_{02}, \Psi_{12}, \Psi_{01}, A_{01}) \to (-\Psi_{11}, \theta_{02}, \Psi_{12}, -\Psi_{01}, -A_{01})$

completely new periodic orbit, or exactly the same periodic orbit, or the same orbit but shifted in phase by half a period (as reflections are idempotent). An orbit affected in the last manner by m will be invariant under the spatio-temporal symmetry $t_m = m t_e$. Fixed points and periodic orbits are characterised by the symmetry operations that leave them invariant.

3. Reduction to ODE models

We construct a low-order model by truncating the PDEs (2.1)–(2.3), extending the treatment of Howard & Krishnamurti (1986) to the magnetic case. Ordinary untilted convection is represented by modes, like $\Psi \propto \sin kx \sin \pi z$, whose amplitudes are invariant under the symmetry m. Horizontal shear is described by $\sin \pi z$ (invariant under l), and nonlinear interactions between these two modes generate $\cos kx \sin 2\pi z$ (invariant under m'), which gives the rolls a tilted appearance. We therefore pose the eleven-mode minimal truncation that imposes point symmetry:

$$\Psi = \Psi_{11} \sin kx \sin \pi z + \Psi_{01} \sin \pi z + \Psi_{12} \cos kx \sin 2\pi z, \tag{3.1}$$

$$\theta = \theta_{11} \cos kx \sin \pi z + \theta_{02} \sin 2\pi z + \theta_{12} \sin kx \sin 2\pi z, \tag{3.2}$$

$$\begin{aligned} A = {} & A_{11} \sin kx \cos \pi z + A_{20} \sin 2kx \\ & + A_{01} \cos \pi z + A_{12} \cos kx \cos 2\pi z + A_{10} \cos kx, \end{aligned} \tag{3.3}$$

where the mode amplitudes are functions only of time. The subscripts refer to the x and z spatial wave numbers. The actions of the spatial symmetries on five of the mode amplitudes are given in Table 2. Substituting the truncation into the PDEs yields an eleventh-order set of ODEs:

$$\begin{aligned} \dot{\Psi}_{11} = {} & -\sigma k_{11}^2 \Psi_{11} + \frac{\sigma k R}{k_{11}^2} \theta_{11} - \sigma \zeta Q \pi A_{11} - \frac{k\pi}{2k_{11}^2}(k^2 + 3\pi^2)\Psi_{01}\Psi_{12} \\ & + \sigma \zeta Q \frac{k\pi}{2k_{11}^2}\left\{ 2(\pi^2 - 3k^2)A_{11}A_{20} + 2(\pi^2 - k^2)A_{01}A_{10} + (k^2 + 3\pi^2)A_{01}A_{12} \right\}, \end{aligned}$$

$$\dot{\theta}_{11} = k\Psi_{11} - k_{11}^2 \theta_{11} + \tfrac{1}{2}k\pi \left\{ 2\Psi_{11}\theta_{02} + \Psi_{01}\theta_{12} \right\},$$

$$\dot{A}_{11} = \pi\Psi_{11} - \zeta k_{11}^2 A_{11} - \tfrac{1}{2}k\pi \left\{ 2\Psi_{11}A_{20} + \Psi_{01}A_{12} + \Psi_{12}A_{01} + 2\Psi_{01}A_{10} \right\},$$

$$\dot{\theta}_{02} = -4\pi^2 \theta_{02} - \tfrac{1}{2}k\pi\Psi_{11}\theta_{11},$$

$$\dot{A}_{20} = -4\zeta\pi^2 A_{20} + \tfrac{1}{2}k\pi \left\{ \Psi_{11}A_{11} - 2\Psi_{12}A_{12} \right\},$$

$$\begin{aligned} \dot{\Psi}_{12} = {} & -\sigma k_{12}^2 \Psi_{12} - \frac{\sigma k R}{k_{12}^2}\theta_{12} - 2\sigma\zeta Q\pi A_{12} + \frac{k\pi}{2k_{12}^2}k^2\Psi_{11}\Psi_{01} \\ & + \sigma\zeta Q \frac{k\pi}{2k_{12}^2}\left\{ k^2 A_{01}A_{11} + (12k^2 - 16\pi^2)A_{12}A_{20} \right\}, \end{aligned} \tag{3.4}$$

$$\dot{\theta}_{12} = -k\Psi_{12} - k_{12}^2 \theta_{12} - \tfrac{1}{2}k\pi\Psi_{01}\theta_{11},$$

$$\dot{A}_{12} = 2\pi\Psi_{12} - \zeta k_{12}^2 A_{12} + \tfrac{1}{2}k\pi\left\{\Psi_{01}A_{11} - \Psi_{11}A_{01} + 4\Psi_{12}A_{20}\right\},$$

$$\dot{A}_{10} = -\zeta k^2 A_{10} + \tfrac{1}{2}k\pi\left\{\Psi_{01}A_{11} + \Psi_{11}A_{01}\right\},$$

$$\dot{\Psi}_{01} = -\sigma\pi^2\Psi_{01} - \sigma\zeta Q\pi A_{01} + \tfrac{3}{4}k\pi\Psi_{11}\Psi_{12} + \sigma\zeta Q\tfrac{1}{2}k\pi\left\{A_{11}A_{10} - \tfrac{3}{2}A_{11}A_{12}\right\},$$

$$\dot{A}_{01} = \pi\Psi_{01} - \zeta\pi^2 A_{01} + \tfrac{1}{2}k\pi\left\{-\Psi_{11}A_{10} + \tfrac{1}{2}\Psi_{12}A_{11} + \tfrac{1}{2}\Psi_{11}A_{12}\right\},$$

where $k_{1n}^2 = k^2 + n^2\pi^2$. This system includes as subsystems the Lorenz (1963) equations and the equations of Howard & Krishnamurti (1986) for convection without a magnetic field; in addition, the fifth-order truncated model of magnetoconvection without shear of Knobloch $et\ al$ (1981) is an m-invariant subsystem. Lantz (1995) has studied the analogous truncated model for sheared convection in a horizontal field.

The number of parameters and equations is reduced by considering the limit of narrow rolls: $L = \pi/k \to 0$ (Hughes & Proctor 1990). Taking this limit is justified by numerical experiments on the PDEs and the analysis of the stability of the unsheared fixed point in (3.4), both of which show that the instability to shearing behaviour occurs most readily in narrow rolls. Indeed, without a magnetic field, we have shown that the shearing instability from symmetric rolls will only occur in the PDEs with $L \lesssim 0.5$, while convection sets in with $L = \sqrt{2}$. Taking the limit $L \to 0$ also has the advantage of reducing the order of the model from eleven to five while retaining the essential dynamics.

The following scalings lead to an appropriate balance between the linear and nonlinear terms:

$$\Psi_{11} \sim \Psi_{01} \sim \Psi_{12} \sim A_{01} \sim L, \quad \theta_{11} \sim \theta_{02} \sim \theta_{12} \sim L^2, \quad A_{11} \sim A_{12} \sim A_{10} \sim L^3. \quad (3.5)$$

Time t and Chandrasekhar number Q are not scaled by any power of L. We expand R about R_C, the Rayleigh number at which the trivial solution first becomes unstable to steady convection:

$$R = R_C(1 + L^2\mu), \qquad \text{where} \qquad R_C = \frac{\pi^4(1+L^2)^3}{L^4} + \pi^2(1+L^2)Q. \quad (3.6)$$

The parameter R (and equivalently μ) is the principal bifurcation parameter. For later convenience, we define alternate Rayleigh and Chandrasekhar numbers r and q by the relations

$$R = \frac{\pi^4(1+L^2)^3}{L^4}r \qquad \text{and} \qquad Q = \frac{\pi^2(1+L^2)^2}{L^4}q. \quad (3.7)$$

R_C is minimised as a function of L when $L^2 = 2/(1+q)$. Thus with no magnetic field, steady convection sets in first with $L = \sqrt{2}$, when $R = 27\pi^4/4$, and strong magnetic fields leads to narrow rolls being preferred at the onset of convection.

With the scalings in (3.5), the six variables θ_{11}, A_{11}, θ_{12}, A_{12}, A_{10} and A_{20} are slaved to the other five variables. Time, the parameter μ and the five variables are redefined to give a tidier set of equations:

$$t \to t/4\pi^2, \quad \mu \to \frac{4(1+\sigma)}{\sigma}\mu, \quad \Psi_{11} \to \sqrt{\frac{32(1+\sigma)}{\sigma}}\Psi_{11}, \quad \Psi_{01} \to 8\Psi_{01},$$

$$\theta_{02} \to \frac{4(1+\sigma)}{\sigma\pi}\theta_{02}, \quad \Psi_{12} \to \sqrt{\frac{32(1+\sigma)}{\sigma}}\Psi_{12}, \quad A_{01} \to \frac{8}{\zeta\pi}A_{01}; \qquad (3.8)$$

Table 3. Fixed points and their spatial symmetry groups. The multiplicity of each fixed point is indicated; angle brackets denote the group generated by the given symmetry operations.

Fixed point	Defining equation	Spatial symmetry group
Trivial (1)	all modes $= 0$	$D_2 = \langle m, l \rangle$
SS (2)	$\Psi_{12} = \Psi_{01} = A_{01} = 0$	$Z_2 = \langle m \rangle$
STC (4)	—	—

this scaling yields the set of model equations (Rucklidge & Matthews 1993):

$$\dot{\Psi}_{11} = \mu \Psi_{11} + \Psi_{11}\theta_{02} - \Psi_{01}\Psi_{12},$$

$$\dot{\theta}_{02} = -\theta_{02} - \Psi_{11}^2,$$

$$\dot{\Psi}_{12} = -\nu \Psi_{12} + \Psi_{11}\Psi_{01},$$

$$\dot{\Psi}_{01} = -\frac{\sigma}{4}\Psi_{01} - \frac{\sigma Q}{4\pi^2}A_{01} + \frac{3(1+\sigma)}{4\sigma}\Psi_{11}\Psi_{12},$$

$$\dot{A}_{01} = \frac{\zeta}{4}\Psi_{01} - \frac{\zeta}{4}A_{01},$$

(3.9)

where $\nu = (9\sigma/4(1+\sigma)) - \mu$, with $\nu > 0$. This system has an m-invariant subspace $(\Psi_{12} = \Psi_{01} = A_{01} = 0)$, so untilted solutions are represented by Ψ_{11} and θ_{02} alone.

The model can be simplified further by considering the limit of small σ. If we allow μ, σ and ζ all to become small at the same rate, the θ_{02} mode will have a larger decay rate than the other four modes and will be slaved to Ψ_{11}. Making the following additional scalings:

$$t \sim \sigma^{-1}, \quad \Psi_{01} \sim A_{01} \sim \sigma, \quad \Psi_{11} \sim \Psi_{12} \sim \sigma^{\frac{3}{2}}, \quad \theta_{02} \sim \sigma^3, \quad (3.10)$$

defining $\tilde{\mu} = \mu/\sigma$ and $\tilde{\zeta} = \zeta/\sigma$, and eliminating θ_{02} by writing $\theta_{02} = -\Psi_{11}^2 + \mathcal{O}(\sigma)$, we obtain the equations of Hughes & Proctor (1990) extended to the magnetic case:

$$\dot{\Psi}_{11} = \tilde{\mu}\Psi_{11} - \Psi_{01}\Psi_{12} - \sigma^2\Psi_{11}^3 + \mathcal{O}(\sigma^3),$$

$$\dot{\Psi}_{12} = -\left(\frac{9}{4} - \tilde{\mu}\right)\Psi_{12} + \Psi_{11}\Psi_{01} + \mathcal{O}(\sigma),$$

$$\dot{\Psi}_{01} = -\frac{1}{4}\Psi_{01} - \frac{Q}{4\pi^2}A_{01} + \frac{3}{4}\Psi_{11}\Psi_{12} + \mathcal{O}(\sigma),$$

$$\dot{A}_{01} = \frac{\tilde{\zeta}}{4}\Psi_{01} - \frac{\tilde{\zeta}}{4}A_{01}.$$

(3.11)

We have retained the $\mathcal{O}(\sigma^2)$ term in the $\dot{\Psi}_{11}$ equation since it provides an unsheared fixed point; this fixed point goes to infinity as σ goes to zero (Moore & Weiss 1973), but still may influence the dynamics for non-zero σ since m-invariant trajectories would otherwise have unbounded growth of Ψ_{11}.

4. Notation for fixed points, periodic orbits and bifurcations

One feature of this problem is the large number of fixed points and periodic orbits. Fixed points are summarised in Table 3: the trivial solution has the full spatial
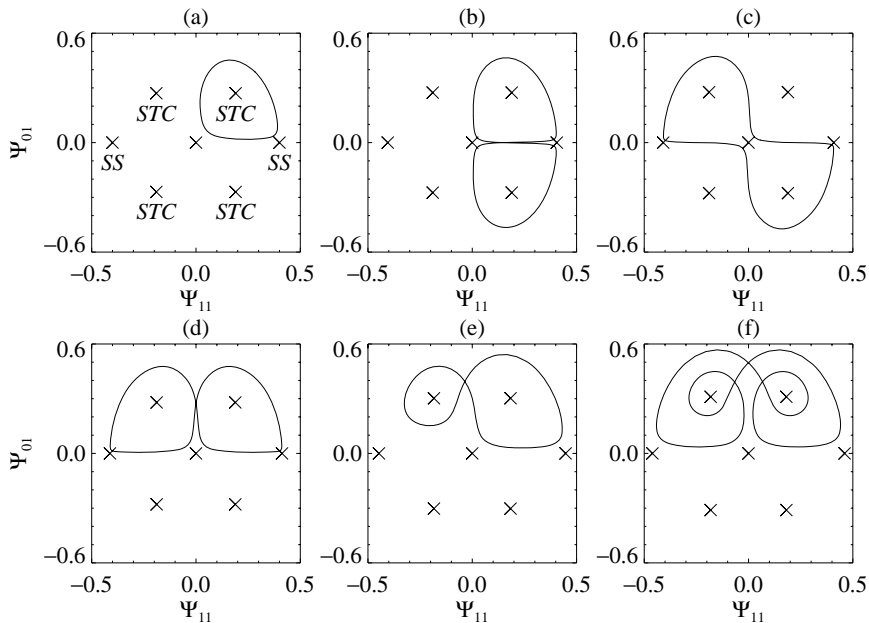
Figure 2. Periodic orbits and their spatio-temporal symmetries. Phase portraits have Ψ_{11} (the roll amplitude) on the horizontal axis and Ψ_{01} (the shear) on the vertical axis. The trivial, SS and STC fixed points are indicated by crosses. The orbits and symmetries are: (a) OTC, with no symmetries; (b) PW, invariant under t_m; (c) PW', invariant under $t_{m'}$; (d) HK, invariant under t_l; (e) AHK, with no symmetries; (f) $(\text{HK})^2$, invariant under t_l. Only one of several periodic orbits that map to each other under the symmetry operators is shown in each case.

symmetry group, steady symmetric (SS) convection is invariant under the reflection m, and steady tilted convection (STC) has no symmetry. Periodic orbits are illustrated in Figure 2. Oscillatory tilted convection (OTC) has no symmetry, but there are three types of symmetric periodic orbit: pulsating waves of two types (PW and PW') and orbits of the type described by Howard & Krishnamurti (1986), which we denote by HK. Pulsating waves (Figure 1) have two rolls in the periodic box that dominate alternately over the cycle, while in PW', it is always the same roll that dominates as the shear reverses. In HK oscillations, the rolls dominate alternately but the shear does not reverse. The prefix letter A indicates a symmetry-broken orbit (e.g., AHK in Figure 2e) and there are doubled orbits such as $(\text{HK})^2$, and so on. Bifurcations (pitchfork, symmetry-breaking, period-doubling, saddle-node and homoclinic) are abbreviated thus: pf, sb, pd, sn and h, and are prefixed by the name of the orbit involved, so, for example, OTC-sn indicates a saddle-node bifurcation involving OTC orbits.

5. The non-magnetic shearing instability

Before launching in to a study of the full magnetic problem, it is important to understand the behaviour in the non-magnetic case, so that we can determine how the behaviour is influenced by the magnetic field, and so that we can identify parameter

values where the non-magnetic behaviour is simple enough that it does not obscure the magnetic effects. Unfortunately, if the aspect ratio L is set at the value that minimises the critical Rayleigh number R_C with no magnetic field ($L = \sqrt{2}$), then the instability to 2D shearing behaviour does not occur in the PDEs before other instabilities have set in. We therefore set $L = 0.5$, in anticipation of the preference for narrow rolls in the presence of a magnetic field; all our calculations suggest that some narrowing of the rolls is required for the shearing instabilities to take place.

5.1. Overview of the simplest case

We begin with the analysis of the non-magnetic ($Q = 0$) version of the narrow-roll fifth-order model (3.9), repeated here for convenience:

$$
\begin{aligned}
\dot{\Psi}_{11} &= \mu\Psi_{11} + \Psi_{11}\theta_{02} - \Psi_{01}\Psi_{12}, \\
\dot{\theta}_{02} &= -\theta_{02} - \Psi_{11}^2, \\
\dot{\Psi}_{12} &= -\nu\Psi_{12} + \Psi_{11}\Psi_{01}, \\
\dot{\Psi}_{01} &= -\frac{\sigma}{4}\Psi_{01} + \frac{3(1+\sigma)}{4\sigma}\Psi_{11}\Psi_{12}.
\end{aligned}
\tag{5.1}
$$

The equations have an m-invariant subspace: $\Psi_{12} = \Psi_{01} = 0$. The trivial solution has real eigenvalues (μ, -1, $-\nu$ and $-\frac{1}{4}\sigma$), and loses stability at $\mu = 0$ in a pitchfork bifurcation to a pair of SS fixed points.

For $0 < \mu < 9\sigma/4(1+\sigma)$ (the upper limit is given by the restriction that $\nu > 0$), the one-dimensional unstable manifold of the trivial solution provides a structurally stable connection to the SS fixed points within the invariant subspace. This implies that a heteroclinic bifurcation involving the trivial and SS fixed points may occur with codimension one. Within the invariant subspace, SS are attracting, with stable complex eigenvalues if $\mu > \frac{1}{8}$. The system breaks out of the invariant subspace in a supercritical pitchfork bifurcation to form four STC fixed points when

$$
\mu = \frac{9\sigma^3}{4(1+\sigma)(3+3\sigma+\sigma^2)}.
\tag{5.2}
$$

This expression for μ translates to a prediction of $r \sim 1 + 3\sigma^2 L^2$ for the location of the pitchfork bifurcation from SS to STC in the PDEs, in the limit of small Prandtl number and roll width.

The other way the system could break out of the invariant subspace would be in a Hopf bifurcation from SS leading to pulsating waves, but this does not occur in (5.1) for $\nu > 0$. This Hopf bifurcation occurs in the PDEs, but only for $\sigma \gtrsim 3.5$ when $L = 0.5$ (see below).

The STC fixed points undergo a Hopf bifurcation to OTC (Figure 3a), which collide with the SS and trivial fixed points simultaneously (b) and glue together; beyond this heteroclinic bifurcation, there are a pair of HK orbits (c). These periodic orbits have the symmetry t_l (so symmetry is increased in this gluing bifurcation), and the sign of the shear Ψ_{01} does not change. The remainder of this section is concerned with the different global bifurcations that may take the place of the simple heteroclinic gluing bifurcation described here.
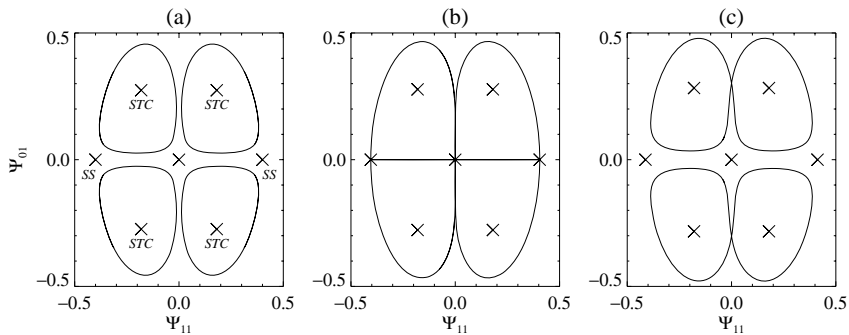
Figure 3. The global bifurcation in (5.1) (no magnetic field), with $\sigma = 0.5$. The four OTC periodic orbits in (a) $\mu = 0.16$ collide with the trivial and SS fixed points near (b) $\mu = 0.163875$, with two HK periodic orbits emerging in (c) $\mu = 0.17$.
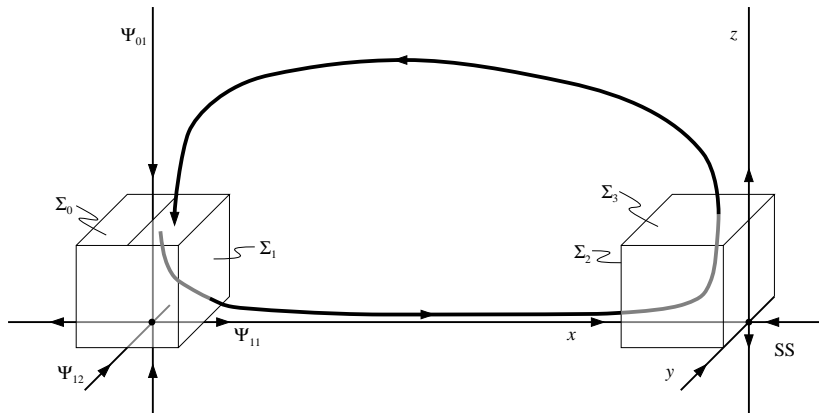

Figure 4. The trajectory starts (on the left) near the origin on the plane Σ_0, leaves the box around the origin crossing Σ_1, continues to one of the SS fixed points, enters the box around that fixed point through Σ_2, leaves through Σ_3, then returns to Σ_0.

5.2. Orbits and maps: real eigenvalues

Behaviour beyond the Hopf bifurcation must be determined numerically, and global bifurcations like the one illustrated in Figure 3 are best understood by constructing Poincaré maps. Near global bifurcations, trajectories spend most of their time near the fixed points, and move rapidly between them. Using this separation of time-scales, the flow can be approximated by low-dimensional maps using standard techniques (Guckenheimer & Holmes 1983). When $\sigma < 4\nu$ at the bifurcation, which is true in the model (5.1) when $\sigma \lesssim 2.47$, trajectories approach the origin tangent to the Ψ_{01}-axis. We will show that this implies that non-reversing HK oscillations result after the global bifurcation, while for $\sigma \gtrsim 2.47$, reversing oscillations are found.

We consider a trajectory, depicted in Figure 4, that starts near the origin on the plane Σ_0 defined by $|\Psi_{01}| = h_0$, where h_0 is a small positive constant; we follow this trajectory as it passes the origin, travels out to one of the two SS fixed points, and returns to a neighbourhood of the origin, hitting the plane Σ_0 once more. Thus

the flow defines a map from this plane back to itself. This map may be calculated approximately by considering small boxes around each of the fixed points: within these boxes, the flow is approximately linear and is dominated by the eigenvalues of the fixed points, and between the boxes, the flow can be linearised about the one-dimensional unstable manifolds of the fixed points.

The OTC orbits collide with the trivial and the SS fixed points simultaneously because the leading stable direction at SS is tangent to the structurally stable heteroclinic connection from the trivial fixed point to SS within the m-invariant subspace, and almost all trajectories that hit SS must do so tangent to the leading direction. This forces the OTC periodic orbits to hit the invariant line that connects the trivial and SS fixed points. This situation holds in the model (5.1) for all parameter values of interest, but we shall see below that either increasing σ in the PDEs or adding a magnetic field will allow a leading stable direction that is not in the m-invariant subspace; in those cases, periodic orbits need not collide with the trivial and SS fixed points simultaneously, and the global bifurcations will be quite different.

The construction of the map proceeds in the standard fashion, but we will treat the derivation in some detail as this is the simplest case considered in this paper. We define four planar sections Σ_0 to Σ_3 (see Figure 4): Σ_0 ($|\Psi_{01}| = h_0$) and Σ_1 ($|\Psi_{11}| = h_1$) are close to the trivial solution, where the flow is approximately

$$\dot{\Psi}_{11} = \mu \Psi_{11}, \qquad \dot{\theta}_{02} = -\theta_{02}, \qquad \dot{\Psi}_{12} = -\nu \Psi_{12}, \qquad \dot{\Psi}_{01} = -\frac{\sigma}{4} \Psi_{01}. \qquad (5.3)$$

By rescaling the variables, we set $h_0 = h_1 = 1$ in the maps throughout. The flow defines a map T_0 from Σ_0 to Σ_1:

$$T_0 (\Psi_{11}^0, \theta_{02}^0, \Psi_{12}^0, \Psi_{01}^0 = \pm 1) = (\text{sgn}(\Psi_{11}^0), \theta_{02}^0 |\Psi_{11}^0|^{1/\mu}, \Psi_{12}^0 |\Psi_{11}^0|^{\nu/\mu}, \pm |\Psi_{11}^0|^{\sigma/4\mu}), \quad (5.4)$$

where we note that Σ_1 includes Ψ_{11} positive and negative; we take $\Psi_{11} > 0$ for the moment. The superscript 0 refers to the plane Σ_0.

We define local coordinates (x, y, z, w) around the SS fixed point (on the right in Figure 4) such that in these coordinates, the Jacobian matrix at SS is block diagonal. The coordinates x and y are in the m-invariant subspace, while z and w are linear combinations of Ψ_{12} and Ψ_{01} with the eigenvalue in the z direction positive and the eigenvalue in the w direction negative. We chose z such that $z > 0$ when $\Psi_{01} > 0$. The two remaining planes are Σ_2 ($x = h_2$) and Σ_3 ($|z| = h_3$). Again, by rescaling, we may set $h_2 = h_3 = 1$. For now, we consider only the case $\mu < \frac{1}{8}$, so the flow near that point is governed by

$$\dot{x} = \lambda_1^- x, \qquad \dot{y} = \lambda_2^- y, \qquad \dot{z} = \lambda^+ z, \qquad \dot{w} = \lambda_3^- w, \qquad (5.5)$$

where the λ's are the eigenvalues of the Jacobian, with λ^+ positive and the other three negative. We choose x and y such that $\lambda_2^- < \lambda_1^- < 0$.

The map T_1 from Σ_1 to Σ_2 is linearised about the unstable manifold of the origin, which stays within the m-invariant subspace. The symmetry with respect to changing the signs of Ψ_{12} and Ψ_{01} (along with z and w) simultaneously means that the most general form of the linear map is

$$T_1 (1, \theta_{02}^1, \Psi_{12}^1, \Psi_{01}^1) = (1, A_1 + A_2 \theta_{02}^1, B_1 \Psi_{12}^1 + B_2 \Psi_{01}^1, C_1 \Psi_{12}^1 + C_2 \Psi_{01}^1). \qquad (5.6)$$

where A_1, A_2 etc. are constants that depend on the flow between Σ_1 and Σ_2. The linear flow near SS defines the map T_2 from Σ_2 to Σ_3:

$$T_2(1, y_2, z_2, w_2) = (|z_2|^{-\lambda_1^-/\lambda^+}, y_2|z_2|^{-\lambda_2^-/\lambda^+}, \operatorname{sgn}(z_2), w_2|z_2|^{-\lambda_3^-/\lambda^+}) \quad (5.7)$$

The trajectory can return to the neighbourhood of the trivial fixed point along either branch of the unstable manifold of the SS fixed point, depending on the sign of z_2. We define Γ_+ to be the branch of the unstable manifold of SS with $\Psi_{11} > 0$ that leaves the neighbourhood of that fixed point with Ψ_{01}, or equivalently, z, positive. Similarly, Γ_- leaves with Ψ_{01} negative: $\Gamma_- = m\Gamma_+$. These two branches of the unstable manifold of SS $\Gamma_\pm$ leave the neighbourhood of SS with $z = \pm 1$ and intersect the plane Σ_0 at $(-\kappa, \alpha, \pm\beta, \pm 1)$, where α and β are constants that depend on the global flow. The heteroclinic bifurcation occurs when Γ_+ returns exactly to the trivial fixed point, entering its stable manifold; this occurs when $\kappa = 0$. Thus κ in the map controls the proximity to the heteroclinic bifurcation and increases through zero as μ and r increase through the primary heteroclinic bifurcation. The most general form of the map linearized about the unstable manifold is

$$T_3(x_3, y_3, \pm 1, w_3) = (-\kappa + E_1 x_3 + E_2 y_3 \pm E_3 w_3, \alpha + F_1 x_3 + F_2 y_3 \pm F_3 w_3,$$
$$\pm \beta \pm G_1 x_3 \pm G_2 y_3 + G_3 w_3, \pm 1), \quad (5.8)$$

where E_1 etc. are constants.

Composing these four maps results in a three-dimensional map T from the plane Σ_0 back to itself, which can be simplified in several ways if the parameter values are such that the system is close enough to the global bifurcation. In this case, the value of Ψ_{11} at the beginning of the cycle will be small; this small number is raised to three different powers in the map T_0 (5.4), and the term with the power closest to zero will be largest after that map. In the case of interest here, the Ψ_{01} term dominates, since $\frac{1}{4}\sigma < \nu < 1$, so we need only retain that term in T_0 and T_1:

$$T_0(\Psi_{11}^0, *, *, \pm 1) \approx (\operatorname{sgn}(\Psi_{11}^0), *, *, \pm |\Psi_{11}^0|^{\sigma/4\mu}) \quad (5.9)$$

and

$$T_1(1, *, *, \Psi_{01}^1) \approx (1, A_1, B_2 \Psi_{01}^1, C_2 \Psi_{01}^1). \quad (5.10)$$

Here, $*$ indicates that the value does not matter, near enough to the global bifurcation. Similarly, the x term dominates the y term near SS; in addition, for parameter values of interest at the moment, it dominates the w term, so T_2 and T_3 can be simplified to

$$T_2(1, *, z_2, *) \approx (|z_2|^{-\lambda_1^-/\lambda^+}, *, \operatorname{sgn}(z_2), *) \quad (5.11)$$

and

$$T_3(x_3, *, \pm 1, *) \approx (-\kappa + E_1 x_3, *, *, \pm 1). \quad (5.12)$$

Under these circumstances, the composed map T from Σ_0 back to itself simplifies to

$$T(\Psi_{11}^0, *, *, 1) \approx (\operatorname{sgn}(\Psi_{11}^0)(-\kappa + E|\Psi_{11}^0|^{\delta_T \delta_{SS}}), *, *, \operatorname{sgn}(B_2)), \quad (5.13)$$

where $\delta_T = \sigma/4\mu$, $\delta_{SS} = -\lambda_1^-/\lambda^+$ and we have collected all constants together into one parameter E and extended to the case of Ψ_{11} negative. Thus the essential dynamics near the global bifurcation is governed by a one-dimensional map that we recognise as the Lorenz map (see Sparrow 1982):

$$\Psi_{11} \to f(\Psi_{11}) = \mathrm{sgn}(\Psi_{11})(-\kappa + E|\Psi_{11}|^\delta), \qquad (5.14)$$

where $\delta = \delta_T \delta_{SS}$. The behaviour of the shear variable Ψ_{01} depends only on the sign of the global parameter B_2, which must be positive when it is OTC periodic orbits (which have shear in one direction only) that are involved in the global bifurcation.

To show rigorously that the map (5.14) correctly captures the dynamics of the flow (5.1) would require a proof of the existence of a strong stable foliation, which provides a new set of coordinates $(\hat{\Psi}_{11}, \hat{\theta}_{02}, \hat{\Psi}_{12})$ of the plane Σ_0 that has the property that lines of constant $\hat{\Psi}_{11}$ are mapped to each other under the flow. We do not undertake this proof; however, numerical experiments show that in this system, close to the global bifurcation and close to the heteroclinic orbit (that is, when κ and Ψ_{11}^0 are small enough), the map (5.14) is an excellent model of the flow, particularly so when δ is close to one. To this end, we return to the model ODEs (5.1) and the PDEs (2.1)–(2.3) to explore the parameter regime near the global bifurcation with $\delta \approx 1$.

5.3. Global bifurcations in the ODEs and PDEs

Global bifurcations in sets of ODEs can be continued numerically in two parameters by following periodic orbits of very large period using the continuation package AUTO (Doedel & Kernévez 1986). A preferable method is to treat a homoclinic or heteroclinic connection as a boundary value problem (Beyn 1990; Champneys & Kuznetsov 1994); Champneys kindly provided the code that allowed AUTO to continue homoclinic and heteroclinic bifurcations in two parameters and to detect codimension-two global bifurcations. We have followed the primary heteroclinic bifurcation in the ODEs, which was illustrated in Figure 3, to smaller μ (see Figure 5); it begins with $\delta > 1$, but crosses into region where $\delta < 1$ at a codimension-two point (labelled A in Figure 5b) with $(\mu, \sigma) \approx (0.09137, 0.3691)$. With $\delta > 1$, the global bifurcation is a simple gluing bifurcation, converting OTC to HK periodic orbits, but for $\delta < 1$, this gluing bifurcation splits into an infinite series of heteroclinic bifurcations, with a narrow wedge of attracting chaotic trajectories.

This codimension-two point A in the ODEs corresponds in the map (5.14) to the point where there is a global bifurcation ($\kappa = 0$) coincident with $\delta = 1$. The dynamics of the map near this point is well understood (Glendinning 1985, 1988). Examples of such points in other sets of ODEs have been studied (Lyubimov & Zaks 1983; Shil'nikov 1986; Rucklidge 1993), and Rucklidge (1994) has discussed an example of such a point in the PDEs for 2D magnetoconvection (2.1)–(2.3), but in a completely different parameter range from that under study here.

The details of the dynamics near the codimension-two point depend on the parameter E in the map (5.14). When $\delta \neq 1$, Ψ_{11} and κ can be rescaled so that $E = \pm 1$ (so only the sign of E matters), but the scaling is singular when $\delta = 1$. In that case, the actual value of E becomes important: there are critical values of E at which the pattern of bifurcations near the codimension-two point changes (Lyubimov & Zaks 1983). We have not estimated the value of E in the ODEs, but the numerical observation of the splitting of the gluing bifurcation into a wedge of chaotic trajectories as δ decreases through 1 is consistent with $0 < E < 1$ (see Rucklidge 1993).
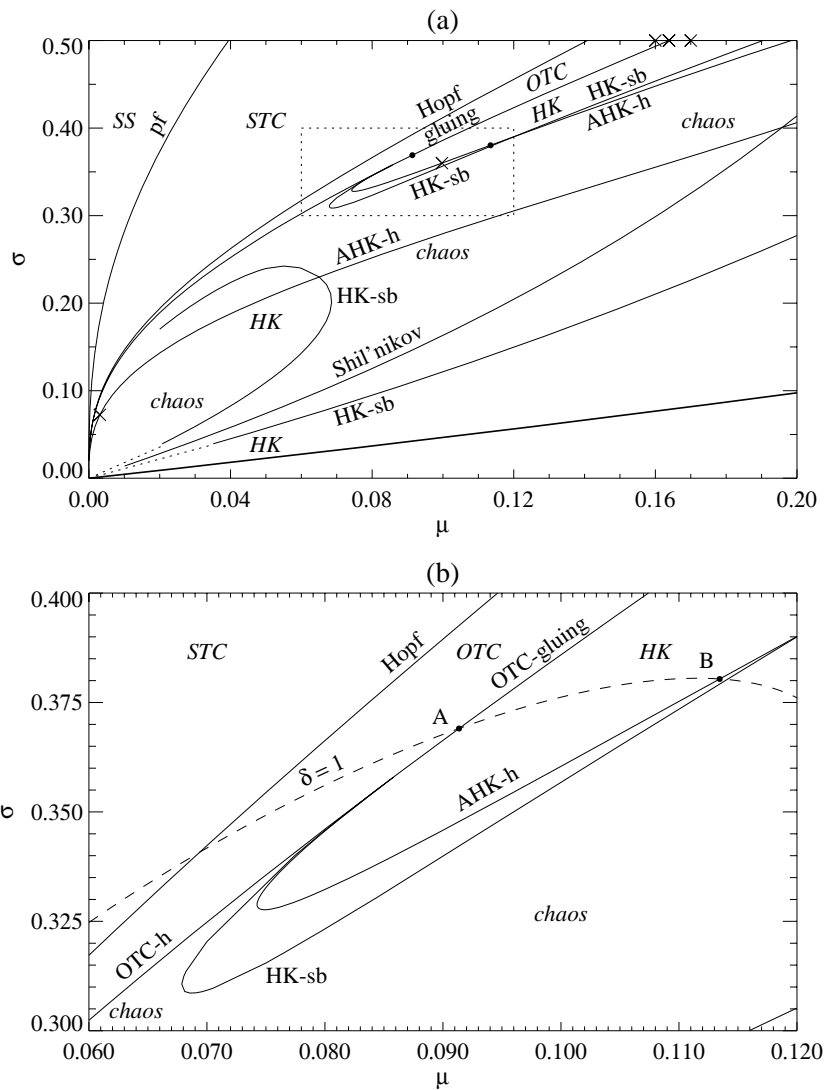
Figure 5. Partial unfolding diagram of the ODEs (5.1). (a) The region $0 \le \mu \le 0.2$ and $0 \le \sigma \le 0.5$. (b) Detail of the region (shown as a dotted box in a) where the gluing bifurcation crosses from $\delta > 1$ (above the broken line) to $\delta < 1$ (below the broken line). The attracting solutions in each parameter region are labelled in italics, and the bifurcation lines are labelled in roman. Two points where heteroclinic bifurcations cross the line $\delta = 1$ are labelled A and B. The thicker line (the lowest line in a) indicates $\nu = 0$, the limit of validity of the ODE model. Crosses in (a) indicate parameter values illustrated in Figure 3 and Figure 6. A line of heteroclinic connections of the Shil'nikov type (between pairs of STC fixed points, which are saddle-foci) is indicated. The two dotted lines in (a) are the locations of HK-symmetry-breaking bifurcations in the ODE model (3.11) (with $Q = 0$).

We have followed three of the bifurcations that emerge from the codimension-two point in the ODEs: two heteroclinic bifurcations (Figure 6), and a symmetry-breaking
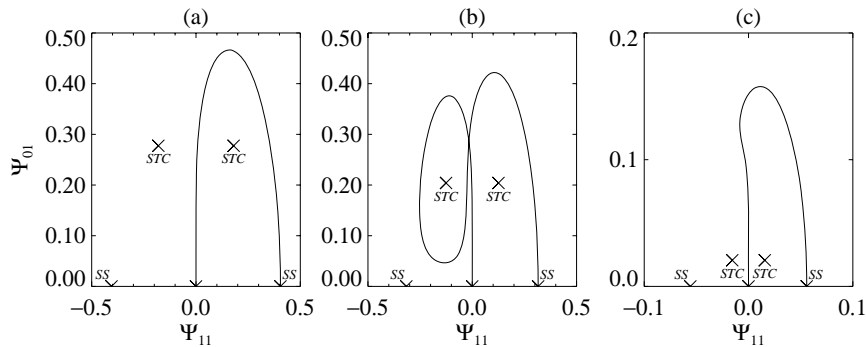
Figure 6. Phase portraits of heteroclinic connections in the ODEs (5.1) at the two heteroclinic bifurcations that were continued numerically. (a) The OTC heteroclinic bifurcation, at $(\mu, \sigma) = (0.16387478, 0.50)$; (b) the AHK heteroclinic bifurcation, at $(\mu, \sigma) = (0.09972241, 0.36)$. (c) the AHK heteroclinic bifurcation, at $(\mu, \sigma) = (0.00311294, 0.07237257)$.

bifurcation at which the HK periodic orbit loses stability to a pair of asymmetric HK (AHK) orbits related to each other by t_l (recall Figure 2). This last bifurcation is subcritical when it begins at the codimension-two point, so the AHK orbits formed are unstable. The line of heteroclinic bifurcations involving OTC orbits, which is labelled OTC-gluing when $\delta > 1$ and OTC-h when $\delta < 1$, continues to $\mu = \sigma = 0$, whereas the lines of HK symmetry-breaking bifurcations (labelled HK-sb) and AHK-heteroclinic bifurcations (AHK-h) both emerge from A, then arch back until they recross the broken line, where $\delta = 1$. The AHK-heteroclinic bifurcation then turns around again (outside the illustrated parameter range) and approaches $\mu = \sigma = 0$; the heteroclinic connection for this range of parameters is illustrated in Figure 6(c).

The value of δ does not affect the symmetry-breaking bifurcation, but the AHK-heteroclinic bifurcation crosses the line $\delta = 1$ at a second codimension-two heteroclinic bifurcation point, which is labelled B in Figure 5(b); near this point, the flow is modelled equally well by the map (5.14), though the T_3 map would include a more elaborate itinerary (as in Figure 6b). Numerical exploration of the ODEs near the AHK heteroclinic bifurcation with $\delta > 1$ reveals a cascade of symmetry-breaking bifurcations, interleaved with symmetry-restoring gluing bifurcations that produce orbits like $(\text{HK})^2$. The cascade accumulates in a chaotic attractor. This gluing cascade with $\delta > 1$, along with the observed presence of attracting chaotic trajectories near the AHK heteroclinic bifurcation with $\delta < 1$, can be described by the Lorenz map (5.14) with $1 < E < 2$ (Arnéodo *et al* 1981; Lyubimov & Zaks 1983).

To illustrate the effect of the OTC and AHK global bifurcations, we take two cuts, shown schematically in Figure 7, through the ODE (μ, σ)-plane. Recall Figure 2 for notation. We choose two values of σ with $\delta > 1$ and $\delta < 1$ at the global bifurcations to demonstrate the possible patterns of behaviour. Rather than show trajectories of the ODE model (5.1) to illustrate these bifurcation sequences, we demonstrate that the model provides a useful guide to understanding the sequence of bifurcations in the PDEs by computing first the local bifurcations in the PDEs, then a sequence of PDE trajectories taken at two values of σ with increasing r to explore global bifurcations. We choose a fixed small aspect ratio $L = 0.5$ $(k = 2\pi)$, so we do not expect quantitative agreement between the PDEs and the ODE model, which was derived in the limit of

(a)

(b)

OTC-gluing

HK

OTC

- - - - - *STC*

Hopf - - - - - *SS*

pf

pf

μ

chaos

AHK-h

HK

OTC-h

HK-sb

OTC-sn

OTC

- - - - - *STC*
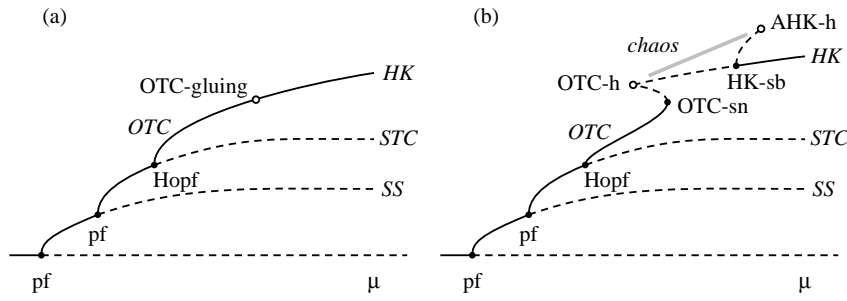
Hopf - - - - - *SS*

pf

pf

μ

Figure 7. Schematic bifurcation diagrams of the ODES (5.1), illustrating the sequence of bifurcations that lead from the trivial solution to HK orbits: amplitude plotted against the bifurcation parameter μ. Local bifurcations, such as pitchfork (pf) and Hopf bifurcations, are indicated with closed circles, while global (gluing, homoclinic or heteroclinic) bifurcations are indicated with open circles; bifurcations are labelled in roman type. Stable and unstable solutions are indicated by solid and broken lines respectively and are labelled in italic type. The diagrams are cuts taken through Figure 5 with (a) $\sigma = 0.385$ ($\delta > 1$) and (b) $\sigma = 0.340$ ($\delta < 1$), with μ increasing. In (a), there is a simple gluing bifurcation from OTC to HK at $\mu \approx 0.099528$ with $\delta \approx 1.06 > 1$, as in the case when $\sigma = 0.5$ (Figure 3). In (b), the simple gluing bifurcation has split into a chaotic wedge (attracting chaotic trajectories exist for $0.07711 \leq \mu \leq 0.07760$), since $\delta \approx 0.91 < 1$. The unstable HK orbits created in the heteroclinic bifurcation at $\mu = 0.07710112$ gain stability at $\mu = 0.07743$ in an HK-symmetry-breaking bifurcation.

narrow rolls. Nonetheless, the qualitative agreement between the two (that is, the order of the bifurcations in the ODEs and PDEs as r increases) turns out to be remarkably good for small σ, considering how far this is from the narrow-roll limit. In comparing the ODEs and PDEs, recall from (3.6) that μ is proportional to $r - 1$.

We have solved the PDEs (2.1)–(2.3) using the spectral code of Rucklidge (1994) extended to include modes that break the symmetry m along the lines of the expansion given in (3.1)–(3.3). We do not include modes that permit travelling waves, so all solutions presented here will be point-symmetric. The code constructs a modestly high order truncation of the PDEs using sines and cosines as basis functions. Wave numbers typically up to 14 in the x and z directions were used; in the calculations reported here, the amplitudes of the highest-order modes did not exceed 10^{-5} times the amplitude of the primary mode. The code also permits the direct numerical determination of the eigenvalues of steady solutions.

The locations of the local (pitchfork, saddle-node and Hopf) bifurcations from the SS and STC fixed points in the non-magnetic PDEs with $L = 0.5$ are shown in Figure 8, as a function of r and σ. The behaviour of the PDEs in the limit $\sigma \to 0$ is captured correctly by the ODE model: the pitchfork bifurcation from SS to STC and the Hopf bifurcation from STC to OTC have critical Rayleigh numbers that scale as $r \sim 1 + \mathcal{O}(\sigma^2)$; the integrations below will confirm that the global bifurcations also follow the behaviour of the ODE model. Agreement between the PDEs and the ODE model should be expected for small σ as the secondary bifurcations occur soon after convection sets in initially and the behaviour will be only weakly nonlinear.

We have explored the global bifurcations in the PDEs in a series of calculations taken with $L = 0.5$ and $\sigma = 0.3$ and 0.5, shown in Figures 9–10. These results
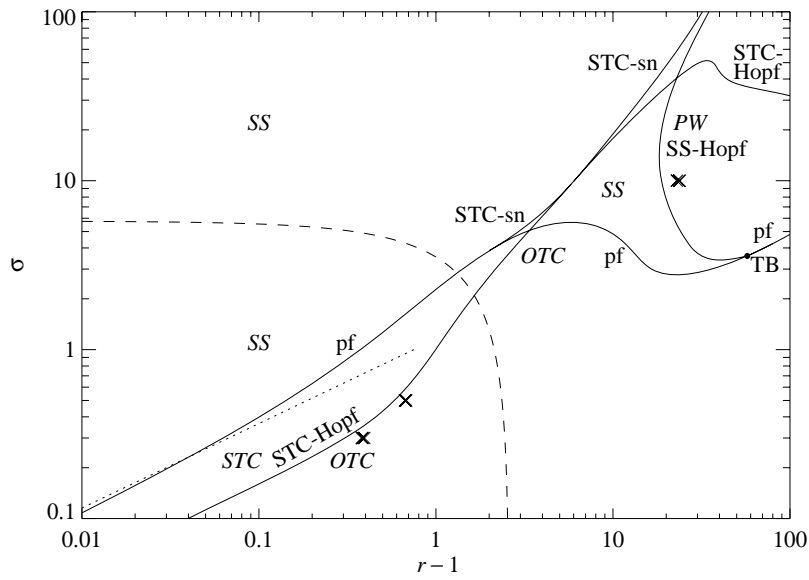
Figure 8. Partial unfolding diagram for the non-magnetic PDEs: the locus of the bifurcations from steady solutions as a function of r and σ, with $L = 0.5$. Wave numbers up to 20 were included in these calculations. The broken line indicates which eigenvalues are dominant (closer to zero) at the origin: below the broken line, Ψ_{01} dominates and we expect HK oscillations after a global bifurcation; above the broken line, Ψ_{12} dominates and we expect PW' oscillations after a global bifurcation. The dotted line is the ODE prediction for the location of the pitchfork bifurcation from SS to STC: $r \sim 1 + 3\sigma^2 L^2$. Crosses indicate parameter values (some quite close together) illustrated in Figures 9–11.
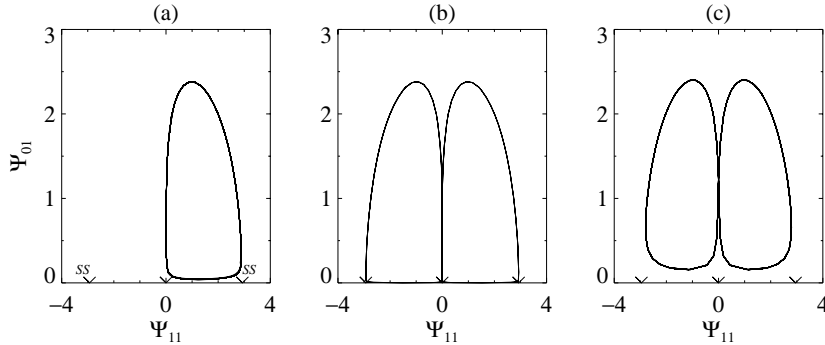
Figure 9. A sequence of phase portraits of the non-magnetic PDEs, with $L = 0.5$ and $\sigma = 0.5$, showing how OTC orbits are converted to HK orbits in a global bifurcation, just as in the ODE model (see Figure 3 and Figure 7a). (a) OTC: $r = 1.670$; (b) HK just past the global bifurcation: $r = 1.67037$; (c) HK: $r = 1.680$. In (b), the relevant ratio of eigenvalues is $\delta \approx 1.12$. The trivial and SS fixed points are indicated by crosses.

should be compared with the ODE behaviour in Figure 7. With $\sigma = 0.5$, there is a
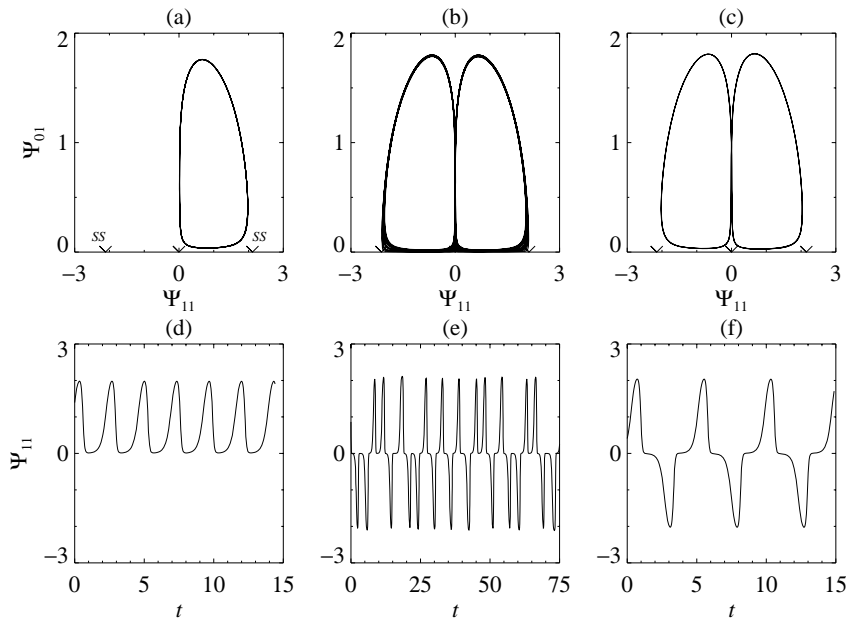
Figure 10. A sequence of phase portraits of the non-magnetic PDEs, with $L = 0.5$ and $\sigma = 0.3$, showing how the gluing bifurcation has split into a chaotic interval (see Figure 7b). (a) OTC: $r = 1.382$; (b) chaos: $r = 1.385$; (c) HK: $r = 1.394$; (d)–(f) are time series corresponding to (a)–(c). In the chaotic interval (b), the relevant ratio of eigenvalues is $\delta \approx 0.70$.

simple gluing bifurcation at $r \approx 1.67037$ (Figure 9); the value of δ at these parameter values is $\delta \approx 1.12$ (greater than one, so we do not expect, and do not find, chaotic trajectories). With $\sigma = 0.3$, this gluing bifurcation has split into an interval of chaotic trajectories (Figure 10), as predicted by the model ODEs (5.1). The value of δ at $r = 1.385$ is $\delta \approx 0.70$, less than one. The time series in Figure 10(d)–(f) correspond to phase portraits in (a)–(c): the irregular changes of sign of Ψ_{11} in Figure 10(e) are the signature of Lorenz chaos. In these oscillations, the direction of the shear never changes, but there are chaotic switches between which of the two rolls in the periodic box dominates. Thus the value of σ below which there is no simple gluing bifurcation is between 0.3 and 0.5 in the PDEs; the ODE model predicts 0.3691, so there is good agreement between the PDEs and Figure 7(a) and (b).

As the Rayleigh number is increased further, we observe in the PDEs the transitions to chaos predicted by the ODE model for larger r, associated with the point B in Figure 5(b). With $\sigma = 0.3$, the HK periodic orbits are stable up to $r = 2.1$, when there is a subcritical symmetry-breaking bifurcation, and the system immediately becomes chaotic, and for higher σ, there are gluing cascades that accumulate in chaotic oscillations.

Clearly the correspondence between the full PDEs, the ODE model and maps derived near global bifurcations could be pursued further. We limit ourselves to a brief discussion of two further cases: smaller σ, where the dynamics is similar to that discussed by Hughes & Proctor (1990), and larger σ, when the first bifurcation from SS in the PDEs is a Hopf bifurcation forming pulsating waves.

5.4. Behaviour for smaller σ

In the ODE model (3.11), which was derived from the PDEs in the limit of narrow rolls and small σ, the linear growth and decay rates are controlled by the single parameter $\tilde{\mu} = \mu/\sigma$ when $Q = 0$. By considering thermosolutal convection, which has two additional parameters, Hughes & Proctor (1990) derived a model with independent linear growth and decay rates and considered the case when the growth rate $\tilde{\mu}$ was very small and the two decay rates ($-\frac{9}{4} + \tilde{\mu}$ and $-\frac{1}{4}$ in this case) were almost equal. The dynamics of their model was heavily influenced by the presence of numerical noise: trajectories approached the m-invariant subspace to within round-off error, so a small numerical error could push trajectories across the invariant subspace. Hughes & Proctor derived a multi-modal one-dimensional map that captured the dynamics of the ODE model both in the presence and in the absence of noise. Lythe (1995) has shown that the same analysis can be carried through even if the decay rates are not equal, as is the case here.

With σ set equal to zero, the cubic term in the $\dot{\Psi}_{11}$ equation of (3.11) vanishes, and there are no SS fixed points. This has the effect that noise-sensitive chaos sets in as soon as $\tilde{\mu}$ is positive. Including a fixed but small σ restores the usual initial sequence of bifurcations (pitchfork to SS, pitchfork to STC then Hopf to OTC when $Q = 0$), but these happen almost immediately, with $\tilde{\mu} = \mathcal{O}(\sigma^2)$. This asymptotic behaviour is recovered in the PDEs (Figure 8). As $\tilde{\mu}$ increases, there follows the interval of noise-sensitive dynamics, but once $\tilde{\mu} \gtrsim \mathcal{O}(\sigma)$, trajectories do not spend time near the m-invariant subspace and the dynamics no longer depends on numerical noise. Subsequent behaviour seems to be independent of σ, so bifurcation values of $\tilde{\mu} = \mu/\sigma$ give the slope with which bifurcation lines approach $(\mu, \sigma) = (0, 0)$ in the unfolding of (5.1) (Figure 5). We have solved the PDEs numerically only for $\sigma = 0.1$ and $k = 2\pi$, and found that the amplitude of the Ψ_{11} mode varies typically over eight orders of magnitude – this range would be greater for smaller values of σ.

5.5. Behaviour for larger σ

In the ODE model (5.1), the leading stable eigenvalues of SS are complex for $\mu > \frac{1}{8}$; with $\sigma = 0.5$ (Figure 3) the heteroclinic bifurcation occurs at $\mu \approx 0.16387478$. It is possible to derive a map for the case of complex eigenvalues at SS using the same construction as was used above. Starting on the plane Σ_0 with a given value of Ψ_{11}, the trajectory returns to the same plane with a new value of Ψ_{11} given by

$$\Psi_{11} \to f(\Psi_{11}) = \mathrm{sgn}(\Psi_{11})(-\kappa + E|\Psi_{11}|^{\delta} \cos(\theta - \delta_i \log |\Psi_{11}|)). \qquad (5.15)$$

Here $\delta = \delta_T \delta_{SS}$, where δ_{SS} is calculated using the real part of the leading stable eigenvalue of SS, $\delta_i = \delta_T \lambda_i / \lambda^+$, where λ_i is the imaginary part of the stable eigenvalue, and E and θ are constants. The same map arises in the context of homoclinic connections from a single saddle-focus to itself (the Shil'nikov scenario); there is simple behaviour (as in the case of real eigenvalues) at the global bifurcation when $\delta > 1$ and complicated behaviour (period-doubling cascades etc.) when $\delta < 1$ (Glendinning & Sparrow 1984; Glendinning 1984). The fact that we have a heteroclinic (rather than homoclinic) connection does not lead to any additional complications in this case. In the ODE model, the transition from $\delta > 1$ to $\delta < 1$ at the global bifurcation (with complex stable eigenvalues) occurs at $(\mu, \sigma) \approx (0.23, 0.61)$, and for $\sigma \gtrsim 0.61$, we observe the expected period-doubling cascades and chaos.
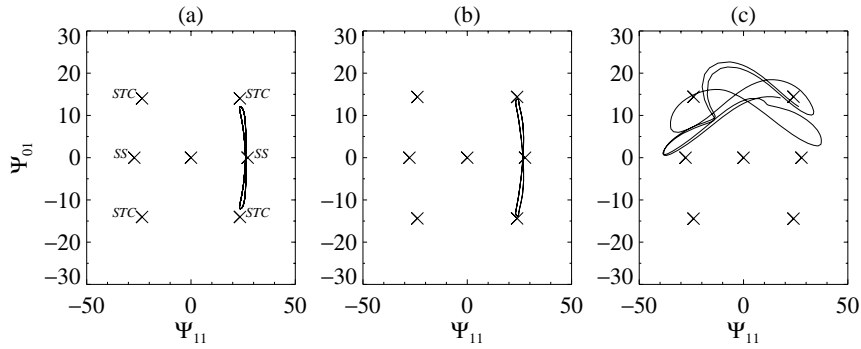
Figure 11. A sequence of phase portraits of the non-magnetic PDEs, with $L = 0.5$ and $\sigma = 10.0$. These integrations were done with wave numbers up to 20 in each direction. (a) Pulsating waves at $r = 24.0$ were created in a Hopf bifurcation from SS at $r = 19.79$. (b) Pulsating waves are destroyed when they collide with the STC fixed points around $r = 24.7$. At this parameter value, STC are saddle-foci with a single real positive eigenvalue and complex leading stable eigenvalues. The unsigned ratio of the positive eigenvalue to the real part of the stable eigenvalues is 0.2265. (c) After this global bifurcation ($r = 24.8$) there are chaotic oscillations in which the sign of the shear does not change.

The derivations of the maps (5.14) and (5.15) above assume that the contraction in the Ψ_{12} direction is strong at the global bifurcation, that is, the Ψ_{01} eigenvalue $-\frac{1}{4}\sigma$ dominates the Ψ_{12} eigenvalue $-\nu$. This condition holds in the ODEs (5.1) at the global bifurcation for $\sigma \lesssim 2.1$; for these values of σ, it is Ψ_{01} that does not change sign in the periodic orbit created in the global bifurcation, while Ψ_{12} does change sign, and an HK orbit is created in the global bifurcation. The Ψ_{12}-direction dominates for larger σ, and it will be the shear Ψ_{01} that changes sign after the global bifurcation. These oscillations with alternating shear are of the type PW'. Thus we expect that the PDEs will have HK oscillations, without reversals of the shear, whenever the shear (Ψ_{01}) eigenvalue dominates the tilt (Ψ_{12}) eigenvalue at the global bifurcation, and that this will occur for smallish σ. Conversely, with larger σ, we expect that the PDEs will have shear reversals beyond the global bifurcation. The transition value of σ in the PDEs occurs when the eigenvalue of Ψ_{01} in (3.4) is equal to the leading eigenvalue in the (Ψ_{12}, θ_{12})-plane, shown as a broken line in Figure 8. Unfortunately, matters are more complicated in this range of σ: not only has the leading direction at the trivial solution changed, but the OTC periodic orbits also approach the STC fixed points, which have complex unstable eigenvalues. As a result, we have not found a clean transition from OTC to PW', though we do find reversals for $\sigma \gtrsim 3$.

For even larger σ, the behaviour of the PDEs is more involved (Figure 8). The pitchfork bifurcation from SS to STC becomes subcritical when $\sigma \approx 4$ and emits a line of STC-saddle-node bifurcations. This line is tangent to the line of STC-Hopf bifurcations when $(r, \sigma) \approx (6.8, 9.5)$. Numerical experiments suggest that a line of bifurcations from OTC to unstable tori begins at this codimension-two Bogdanov bifurcation, which lies in a region where SS are stable. The line of pitchfork bifurcations from SS to STC intersects a line of Hopf bifurcations from SS to PW at a Takens–Bogdanov bifurcation point with Z_2 symmetry at $(r, \sigma) \approx (58.4, 3.59)$; just above this point, the PW created in the Hopf bifurcation are destroyed in a heteroclinic bifurcation with a pair of STC fixed points. We do not pursue these calculations any

further, other than to illustrate how, with $\sigma = 10.0$, pulsating waves (Figure 11a), which were created in a Hopf bifurcation from SS at $r = 19.79$, collide with STC when (b) $r \approx 24.7$ and are replaced by large-amplitude chaotic oscillations (c) in which the shear does not change sign. These last oscillations probably originated in the interaction between the Hopf and saddle-node bifurcations from STC. Prat *et al* (1995) found the Hopf bifurcation to pulsating waves in the related problem of 2D convection between rigid (no-slip) boundaries at the parameter values $k = 2\pi$, $\sigma = 10.0$ and $R = 1.163 \times 10^5$ ($r = 19.87$).

6. The magnetic shearing instability

In the previous section, we studied the global bifurcations in the non-magnetic PDEs and ODE models. Restoring the magnetic field makes matters more complicated as the number of parameters increases by two (Q and ζ) and the dimension of the ODE models increases. We focus on the effects of imposing a weak magnetic field. Periodic orbits will only be perturbed by the magnetic field, but global bifurcations, which are structurally unstable, can be radically altered. We restrict ourselves to the value of σ that had the simplest sequence of bifurcations in the PDEs: with $\sigma = 0.5$ and $Q = 0$, the eigenvalues of the trivial and SS fixed points are real and the eigenvalue ratio δ is greater than one at the primary gluing bifurcation at $r = 1.67037$ (Figure 9). We analyse the ODEs fixing the same value of σ, and although the stable eigenvalues of SS in the m-invariant subspace are complex at the heteroclinic bifurcation, this does not affect the ODE bifurcation structure as these eigenvalues are not leading: their real part is greater in magnitude than the positive and negative eigenvalues out of the m-invariant subspace. We begin with a study of the effect of adding a magnetic field on the map and ODE dynamics, then move on to PDE calculations.

6.1. Eigenvalues of the trivial solution

The eigenvalues of the trivial solution of the ODE model (3.9) are μ, -1, $-\nu$ and $\frac{1}{8}(-(\sigma + \zeta) \pm \sqrt{((\sigma - \zeta)^2 - 4\sigma\zeta Q/\pi^2)})$. The last pair of eigenvalues correspond to the (Ψ_{01}, A_{01})-plane, and there three possibilities for them, shown in Figure 12. If $Q > \pi^2(\sigma - \zeta)^2/4\sigma\zeta$, then the two eigenvalues form a complex pair, but with a smaller magnetic field, the eigenvalues are real and the behaviour of the system is governed by which of the two is closer to zero. The behaviour of these two eigenvalues in the PDEs is identical.

With small Q, the two eigenvalues will be real and close to $-\frac{1}{4}\sigma$ and $-\frac{1}{4}\zeta$, with eigenvectors slightly rotated from the Ψ_{01} and A_{01} axes. We define λ_σ to be the eigenvalue that is closer to $-\frac{1}{4}\sigma$, and similarly λ_ζ. If $\zeta > \sigma$ (region III, Figure 13c), then Ψ_{01} continues to dominate as in the non-magnetic case, and the shear will not reverse in the HK oscillations after the heteroclinic bifurcation.

If $\zeta < \sigma$ (region I in Figure 12), then the leading direction switches discontinuously from the Ψ_{01}-direction ($Q = 0$) to the A_{01}-direction ($Q > 0$). Moreover, the leading eigenvector is not quite in the A_{01}-direction, so as a trajectory approaches the origin, the shear Ψ_{01} may change sign if the trajectory spends enough time in the box around the origin, as illustrated in Figure 13(a). The heteroclinic bifurcation occurs at $\kappa = 0$, when Γ_+, the unstable manifold of the SS fixed point, is within the stable manifold of the origin. As the system approaches the heteroclinic bifurcation, Γ_+ will spend longer and longer in the box around the origin, and there must come a point when the shear
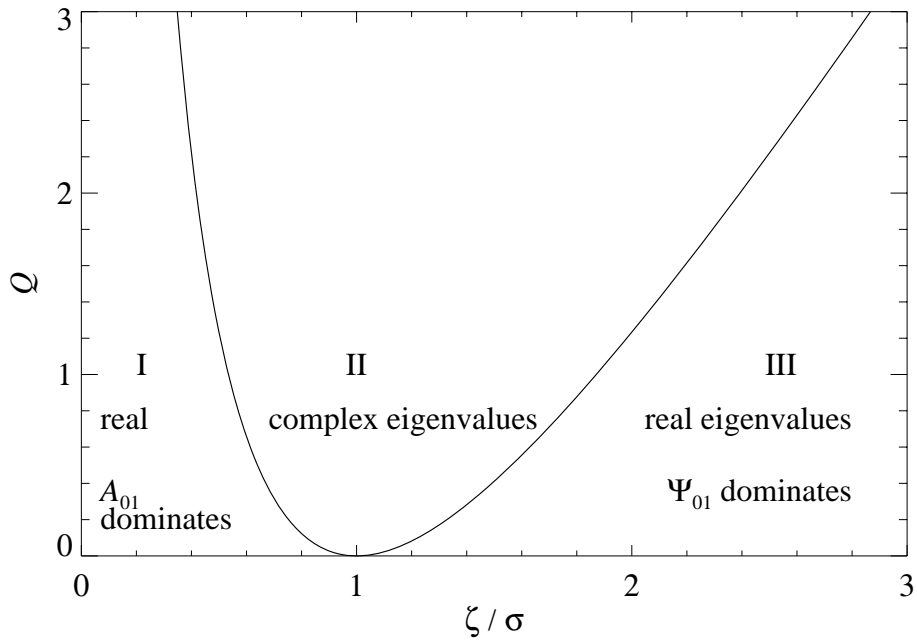
Figure 12. Eigenvalues at the origin in the (Ψ_{01}, A_{01})-plane as a function of ζ/σ and Q: in region II, with $Q > \pi^2(\sigma-\zeta)^2/4\sigma\zeta$ the eigenvalues are complex; otherwise they are real, with A_{01} dominating if $\zeta < \sigma$ (region I) and Ψ_{01} dominating if $\zeta > \sigma$ (region III).
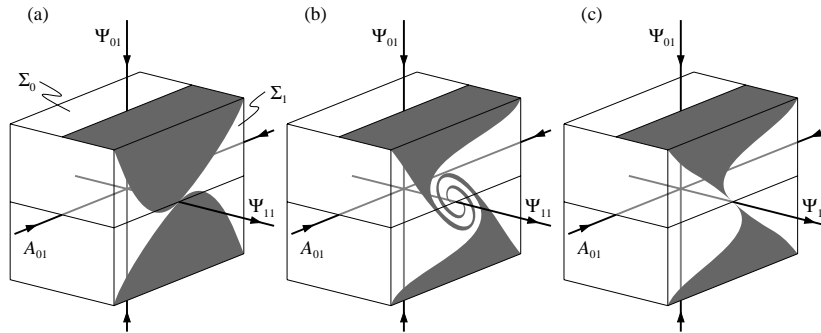

Figure 13. The map T_0 in the parameter regions corresponding to Figure 12: (a) region I: real eigenvalues and $\zeta < \sigma$; (b) region II: complex eigenvalues; (c) region III: real eigenvalues and $\zeta > \sigma$. One half of the plane Σ_0 (shaded region on the tops of the boxes) and the image this region under the symmetry m (on the bottom of the box; not shown) are mapped to the plane Σ_1 (shaded regions on the front of the box). Note how trajectories that begin with $\Psi_{01} > 0$ can end with $\Psi_{01} < 0$ in (a) and (b), but not in (c).

changes sign before it leaves the box. At that point, Γ_+ is in the stable manifold of SS, so there will be a homoclinic bifurcation. Similarly, there is a parameter value after the heteroclinic bifurcation at which Γ_+ enters the stable manifold of the opposite SS

fixed point.

For larger Q or for $\sigma = \zeta$ (region II in Figure 12), the eigenvalues of the origin are complex. As the system approaches the heteroclinic bifurcation at $\kappa = 0$, the shear will change sign an increasing number of times before Γ_+ leaves the box around the origin (Figure 13b); Γ_+ will first acquire a half-twist, so the shear will change sign once. Closer to the heteroclinic bifurcation, Γ_+ will acquire additional half-twists, and for each half twist there will be a parameter value at which there is a homoclinic bifurcation, with Γ_+ returning to the SS fixed point. Thus we expect an infinite sequence of homoclinic bifurcations leading up to the heteroclinic bifurcation at $\kappa = 0$. After the heteroclinic bifurcation ($\kappa > 0$), there will be another infinite sequence of untwisting bifurcations, with Γ_+ hitting the opposite SS fixed point. In the remainder of this section, we discuss the implication of these additional global bifurcations, focusing on region I.

6.2. Local bifurcations

The ODEs have no local bifurcations in the two-dimensional m-invariant subspace aside from the initial pitchfork bifurcation at $\mu = 0$. The pitchfork bifurcation STC occurs at

$$\mu = \frac{9\sigma^3(Q + \pi^2)}{4(1 + \sigma)(3\pi^2(1 + \sigma) + (Q + \pi^2)\sigma^2)} \tag{6.1}$$

and there is also a Hopf bifurcation to pulsating waves, which did not occur with no magnetic field. The pitchfork and the Hopf bifurcations coincide at a Z_2-symmetric Takens–Bogdanov point when Q satisfies the quadratic equation

$$\sigma^2\zeta(Q + \pi^2)^2 + 3\pi^2(\sigma\zeta + \zeta - 9\sigma)(Q + \pi^2) + 27\pi^4(\sigma + \zeta) = 0 \tag{6.2}$$

and μ is given by (6.1). In the ODEs (3.9), with the illustrative parameter values $\sigma = 0.5$ and $\zeta = 0.2$, the two Takens–Bogdanov points occur with $(\mu, Q) \approx (0.0580, 5.024)$ and $(0.6997, 2462.4)$. We shall return to the Takens–Bogdanov point in our discussion of the behaviour with larger magnetic fields, noting that for small Q, the unstable manifold of SS is one dimensional and that there is a structurally stable connection from the origin to the SS fixed points.

6.3. The magnetic map

We construct a map for parameter values close to the non-magnetic heteroclinic bifurcation and for small Q, in order to examine the effect of adding a magnetic field. This construction follows the lines of those in the previous sections; we will retain only Ψ_{11}, Ψ_{01} and A_{01} as the most important variables. As we are aiming to construct a one-dimensional map from Σ_0 back to itself (Figure 4), we will assume that, with small Q, the magnetic field variable A_{01} influences the dynamics only near the origin, providing the mechanism for the reversal of Ψ_{01}, but otherwise it is slaved to Ψ_{01}. This implies that A_{01} takes on the same value ($A_{01} = \pm\gamma$) each time the trajectory hits the plane Σ_0 ($\Psi_{01} = \pm h_0$). Then between Σ_0 and Σ_1 ($|\Psi_{11}| = h_1$), the flow is approximately

$$\dot{\Psi}_{11} = \mu\Psi_{11}, \qquad \dot{\Psi}_{01} = -\frac{\sigma}{4}\Psi_{01} - \frac{\sigma Q}{4\pi^2}A_{01}, \qquad \dot{A}_{01} = \frac{\zeta}{4}\Psi_{01} - \frac{\zeta}{4}A_{01}, \tag{6.3}$$

defining a map T_0 from Σ_0 to Σ_1. The map T_0 is illustrated in Figure 13 for the three parameter regimes defined in Figure 12. In region I, with $\zeta < \sigma$ and Q small, the eigenvalues are real and the magnetic field A_{01} decays most slowly, and it is possible for the shear variable Ψ_{01} to change sign before emerging from the box. A useful approximate form of the map is

$$T_0(\Psi_{11}^0, 1, \gamma) = \left(\mathrm{sgn}(\Psi_{11}^0), |\Psi_{11}^0|^{\delta_\sigma} + AQ(|\Psi_{11}^0|^{\delta_\sigma} - |\Psi_{11}^0|^{\delta_\zeta}), \gamma|\Psi_{11}^0|^{\delta_\zeta}\right), \tag{6.4}$$

where A is a constant, $\delta_\sigma = -\lambda_\sigma/\mu$, $\delta_\zeta = -\lambda_\zeta/\mu$ and γ, assumed constant, is the initial value of A_{01}. The approximation was constructed by requiring that the resulting value of Ψ_{01}^1 be a linear combination of two terms with decay rates λ_σ and λ_ζ having the correct behaviour when $Q = 0$ and changing sign when Ψ_{11}^0 is small enough (provided that $\lambda_\sigma < \lambda_\zeta < 0$). The parameter A in (6.4) could in principle be calculated. We have neglected terms that would affect the sign of the resulting magnetic field A_{01}^1 on the grounds that, for small Q, it is only Ψ_{01} that matters.

In region III, Ψ_{01} does not change sign, and if we neglect terms in Ψ_{01} that decay with rate λ_ζ, we obtain the approximate map

$$T_0(\Psi_{11}^0, 1, \gamma) = \left(\mathrm{sgn}(\Psi_{11}^0), |\Psi_{11}^0|^{\delta_\sigma}, \gamma|\Psi_{11}^0|^{\delta_\zeta}\right). \tag{6.5}$$

We have not included terms that influence the sign of A_{01}^1.

In region II, the eigenvalues of the origin are μ and $\lambda_r \pm i\lambda_i$, and the map T_0 is

$$\begin{aligned} T_0(\Psi_{11}^0, 1, \gamma) = \Big(&\mathrm{sgn}(\Psi_{11}^0), |\Psi_{11}^0|^{\delta_r} \cos\left(\theta_\Psi - \delta_i \log|\Psi_{11}^0|\right), \\ &|\Psi_{11}^0|^{\delta_r} \sin\left(\theta_A - \delta_i \log|\Psi_{11}^0|\right)\Big), \end{aligned} \tag{6.6}$$

where $\delta_r = -\lambda_r/\mu$ and $\delta_i = \lambda_i/\mu$, and the two angles θ_Ψ and θ_A are constants.

The other three maps T_1, T_2 and T_3 are the same for all three parameter regions. The T_1 map includes terms that mix Ψ_{01} and A_{01}, introducing the possibility that Ψ_{01} could change sign between Σ_1 and Σ_2. This mixing can be included in the constants in regions I and II, and the sign of Ψ_{01} does not seem to change in region III, so we do not include such terms in T_1:

$$T_1(1, \Psi_{01}^1, A_{01}^1) = (1, z_2 = \Psi_{01}^1, w_2 = A_{01}^1), \tag{6.7}$$

where we have removed constant factors. Between Σ_2 and Σ_3 near SS, the flow is approximately

$$\dot{x} = \lambda_1^- x, \qquad \dot{z} = \lambda^+ z, \qquad \dot{w} = \lambda_2^- w, \tag{6.8}$$

where x is in the m-invariant subspace. We neglect the fact that SS has complex stable eigenvalues in the m-invariant subspace in the ODEs; in this case, λ_1^- is the real part of those eigenvalues. The map T_2 is

$$T_2(1, z_2, w_2) = (|z_2|^{\delta_1}, \mathrm{sgn}(z_2), w_2|z_2|^{\delta_2}), \tag{6.9}$$

where $\delta_1 = -\lambda_1^-/\lambda^+$ and $\delta_2 = -\lambda_2^-/\lambda^+$. Finally, the map T_3 returns to the plane Σ_0:

$$T_3(x_3, \pm 1, w_3) = (-\kappa + Ex_3 \pm FQw_3, \pm 1, \pm\gamma), \tag{6.10}$$
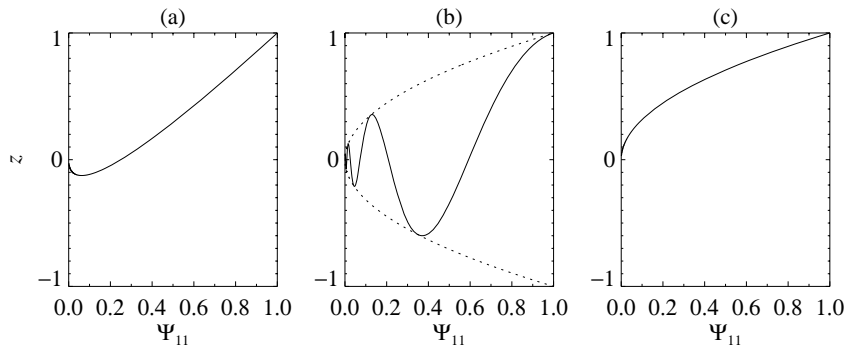
Figure 14. Examples of $z(\Psi_{11})$ (6.13), the value of the shear variable on leaving the neighbourhood of the origin, in (a) region I, (b) region II and (c) region III. Illustrative values are used: (a) $\delta_\sigma = 1.0$, $\delta_\zeta = 0.5$ and $Q = 1.0$; (b) $\delta_r = 0.5$, $\delta_i = 3.0$ and $\theta_\Psi = 0$; (c) $\delta_\sigma = 0.5$. The envelope of the oscillations is shown in (b) by a dotted line.

where E and F are constants. The factor Q is included here as with no magnetic field, the value of w_3 (which is a magnetic field variable) cannot influence the outcome of the map. Composing the four maps leads to a map T from Σ_0 back to itself. We have already dropped the variation in A_{01}, so the map T is a two-dimensional map:

$$T(\Psi_{11}, \Psi_{01} = \pm 1) = (f(\Psi_{11}), \Psi_{01}\, \mathrm{sgn}(z)), \tag{6.11}$$

where we have extended the map to include $\Psi_{01} < 0$, and

$$f(\Psi_{11}) = \mathrm{sgn}(\Psi_{11})\left(-\kappa + E|z|^{\delta_1} + FQ\,\mathrm{sgn}(z)w|z|^{\delta_2}\right). \tag{6.12}$$

The intermediate variables z and w are given by

$$z = \begin{cases} |\Psi_{11}|^{\delta_\sigma} + Q(|\Psi_{11}|^{\delta_\sigma} - |\Psi_{11}|^{\delta_\zeta}) & \text{region I,} \\ |\Psi_{11}|^{\delta_r}\cos\left(\theta_\Psi - \delta_i\log|\Psi_{11}|\right) & \text{region II,} \\ |\Psi_{11}|^{\delta_\sigma} & \text{region III,} \end{cases} \tag{6.13}$$

and

$$w = \begin{cases} |\Psi_{11}|^{\delta_\zeta} & \text{region I,} \\ |\Psi_{11}|^{\delta_r}\sin\left(\theta_A - \delta_i\log|\Psi_{11}|\right) & \text{region II,} \\ |\Psi_{11}|^{\delta_\zeta} & \text{region III.} \end{cases} \tag{6.14}$$

The map (6.11) is strictly-speaking two dimensional, but the Ψ_{01} variable (which represents the sign of the shear) decouples so we can treat it as the one-dimensional map (6.12). A fixed point (with $\Psi_{11} = f(\Psi_{11})$) of (6.12) corresponds to a fixed point of (6.11) when $z(\Psi_{11}) > 0$ and to a period-two point when $z(\Psi_{11}) < 0$ as the shear variable Ψ_{01} changes sign on each iteration.

6.4. Global bifurcations in the ODEs and PDEs

In region III, the map simplifies to

$$T(\Psi_{11}, \Psi_{01} = \pm 1) = \left(\mathrm{sgn}(\Psi_{11})\left(-\kappa + E|\Psi_{11}|^{\delta_\sigma\delta_1} + FQ|\Psi_{11}|^{\delta_\zeta + \delta_\sigma\delta_2}\right), \Psi_{01}\right), \tag{6.15}$$

which gives the same behaviour as the Lorenz map (5.14) in the non-magnetic case. The shear variable Ψ_{01} does not change sign, so the orbits created in the gluing bifurcation or after the interval of chaos are of the HK type.
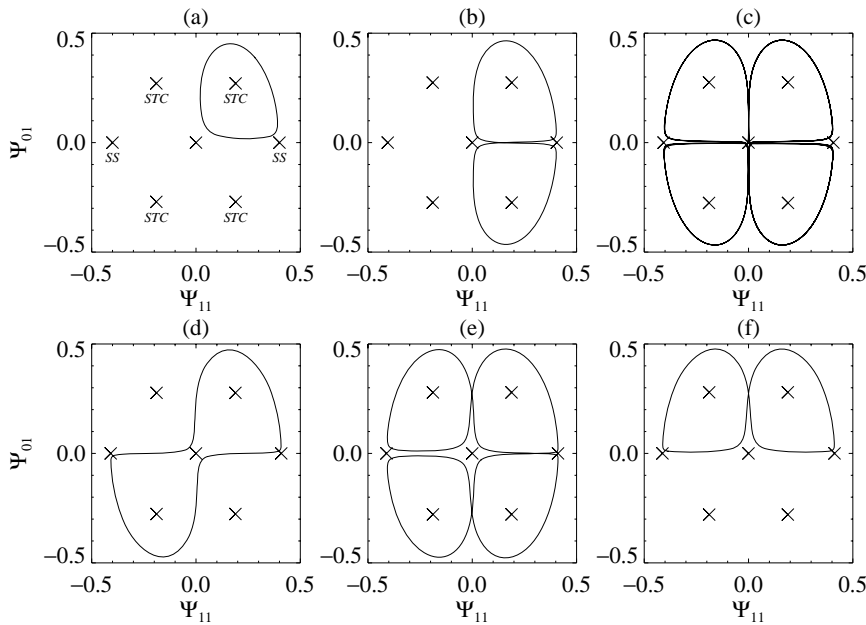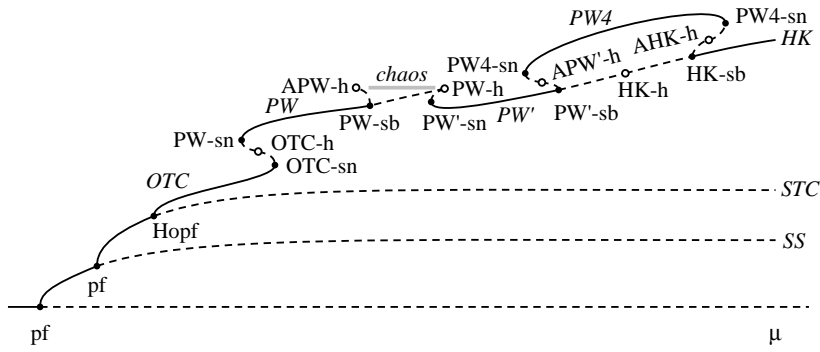
Figure 15. The sequence of global bifurcations in (3.9), with $Q = 1.0$, $\sigma = 0.5$ and $\zeta = 0.2$. Compare with the $Q = 0$ sequence (Figure 3). (a) OTC: $\mu = 0.160$; (b) PW, invariant under t_m: $\mu = 0.164$; (c) chaos: $\mu = 0.1655$; (d) PW′, invariant under $t_{m'}$: $\mu = 0.167$; (e) PW4, invariant under t_m: $\mu = 0.169$; (f) HK, invariant under t_l: $\mu = 0.170$. The eigenvalues at the origin and SS are all real, except for the stable eigenvalues of SS in the m-invariant subspace.

The behaviour in regions I and II is more complicated and is best explained by considering the fate of Γ_+, the branch of the unstable manifold of SS with $\Psi_{11} > 0$. First, Γ_+ hits the plane Σ_0 with $\Psi_{11} = -\kappa$. The z variable, which represents the shear as trajectories leave the origin, is illustrated in Figure 14 for the three parameter regions. These graphs represent z as a function of $\Psi_{11} = -\kappa$, or equivalently, the value of z with which Γ_+ returns to the neighbourhood of the SS fixed point. Each value of κ for which z crosses through zero represents a global bifurcation, as when $z(-\kappa) = 0$, Γ_+ enters the stable manifold of an SS fixed point. In region I, z can only change sign once before leaving the neighbourhood of the origin, while in region II, z changes sign infinitely many times as the global bifurcation is approached (Figure 13a and b).

We begin the discussion of the global bifurcations in region I in the ODE model (3.9) and the PDEs by considering the sequence of orbits of the ODEs depicted in Figure 15, taken with $Q = 1.0$, $\sigma = 0.5$, $\zeta = 0.2$ and μ increasing. The ODE bifurcations (and the analysis of the map) are shown in the schematic diagram in Figure 16. A similar sequence of orbits in the PDEs is shown in Figure 17, with $Q = 0.5$ and the other parameters the same. We focus on the ODE results first, and explain the differences between the ODEs and the PDEs later.

The four OTC periodic orbits in Figure 15(a) collide with the two SS fixed points (but not the trivial solution) and glue together to form two PW (b). Stable OTC and PW orbits coexists over a small parameter interval. At the gluing bifurcation, the ratio of leading stable and unstable eigenvalues of SS is about 0.17; the bifurcation cannot be a simple gluing bifurcation since this value is less than one. Both the leading
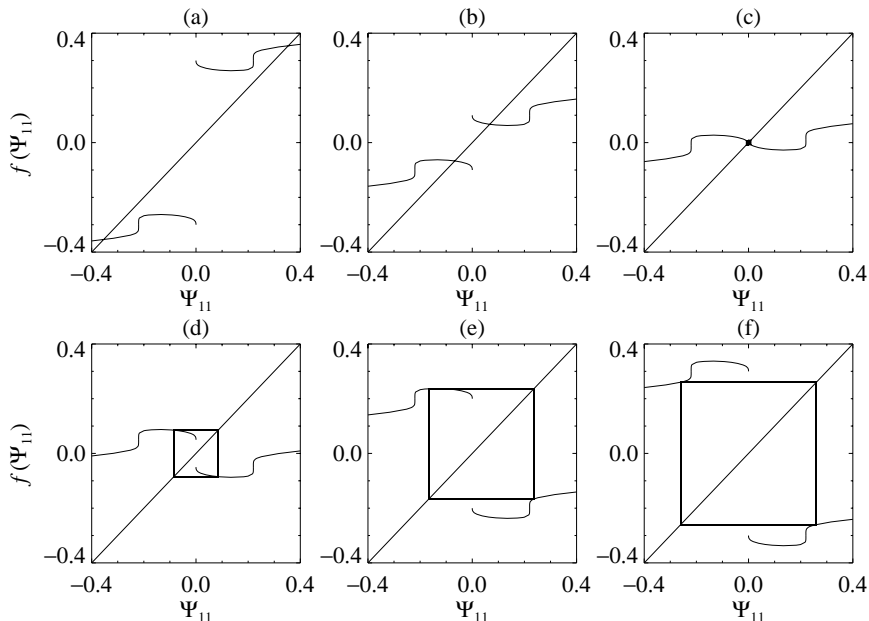
Figure 16. Schematic bifurcation diagram for the ODEs and the PDEs (with some modifications) at the parameter values in Figure 15 and Figure 17. The PDEs do not have an interval of PW4 orbits, but a gluing bifurcation from PW′ to HK, similar to the gluing bifurcation from OTC to PW.

Figure 17. A sequence of orbits in the PDEs, with $Q = 0.5$, $L = 0.5$, $\sigma = 0.5$ and $\zeta = 0.2$, similar to that in the ODEs (Figure 15). These parameter values are in region I. (a) OTC at $r = 1.67$. (b) After a gluing bifurcation: PW at $r = 1.6766$. (c) Chaos at $r = 1.6766019$. (d) Time series corresponding to (c), showing the chaotic changes in the sign of Ψ_{11}. (e) PW′ at $r = 1.67664$. (f) HK at $r = 1.67665$. We have not found PW4 orbits. At the heteroclinic bifurcation ($r \approx 1.6766020$), the relevant ratios of eigenvalues are $\delta_\sigma = 0.4959$, $\delta_\zeta = 0.2242$, $\delta_1 = 2.205$ and $\delta_2 = 0.8345$ (complex).

eigenvalues of SS have eigenvectors in the shear directions that are reversed under the symmetry m. For larger μ, the PW orbits collide with the origin; there is an interval of chaotic trajectories (c), from which a pair of PW′ orbits emerges (d), invariant

Figure 18. Examples of the one-dimensional map (6.12), showing the same sequence as in the ODEs (Figure 15). Parameter values are $E = 0$, $F = 0.1$, $Q = 1$, $\delta_\sigma = 0.7628$, $\delta_\zeta = 0.3051$ and $\delta_2 = 0.1701$. (a) A fixed point (OTC) at $\kappa = -0.30$. (b) After a gluing bifurcation there are PW at $\kappa = -0.10$. This is a period-two point as $z < 0$ at the fixed point and the value of Ψ_{01} (the shear) changes sign at each iteration. (c) Chaotic trajectories at $\kappa = -0.01$. (d) A PW$'$ orbit at $\kappa = 0.05$. (e) A PW4 orbit at $\kappa = 0.20$ (Ψ_{01} changes sign once each time around the period-two orbit, so it in fact period four). (f) An HK orbit at $\kappa = 0.30$.

under $t_{m'}$. The two PW$'$ orbits become unstable before colliding with the two SS fixed points simultaneously; they are replaced by (e) a pair of PW4 orbits. The PW4 orbits are a type of pulsating wave (invariant under t_m) characterised by having two positive excursions of the shear followed by two negative excursions. Finally, each of these two orbits disappears in a saddle-node bifurcation; beyond this point, there are (f) a pair of stable HK orbits, invariant under t_l. These HK orbits were created in the global bifurcation in which PW$'$ were destroyed, and subsequently gained stability in a symmetry-breaking bifurcation.

The initial bifurcations in the PDEs (Figure 17a–c, e) are the same as in the ODEs (Figure 15a–d). There are no PW4 orbits in the PDEs; instead, there is a transition from PW$'$ (Figure 17e) to HK (f) orbits, as in the OTC to PW bifurcation. The two types of transition from PW$'$ to HK orbits seen in the ODEs and in the PDEs have the same net effect, and will be discussed in greater detail below.

6.5. Analysis of the global bifurcations

We analyse these sequences of bifurcations in the ODEs and PDEs using the map (6.11). The behaviour of the system at these global bifurcations depends on the magnitudes of the eigenvalue ratios at the trivial and SS fixed points and on the values of the global parameters E and F. We take as illustrative parameter values the eigenvalue ratios at the heteroclinic bifurcation in the ODEs that occurs with $Q = 0$
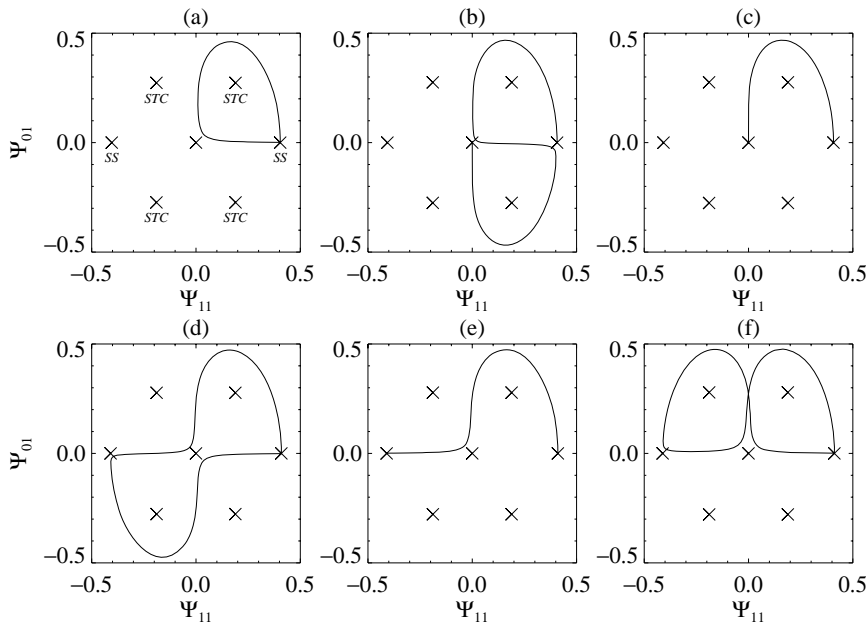
Figure 19. Following Γ_+: homoclinic and heteroclinic connections in the ODEs with $Q = 1.0$, $\sigma = 0.5$ and $\zeta = 0.2$. (a) At the OTC–homoclinic (or gluing) bifurcation: Γ_+ begins at SS and returns there when $\mu = 0.16305092$. (b) At the APW–heteroclinic bifurcation: from SS to the trivial solution at $\mu = 0.16535938$. (c) At the (primary) PW–heteroclinic connection: from SS to the trivial solution at $\mu = 0.16586645$. This corresponds to $\kappa = 0$ in the map (6.12). (d) At the APW′-homoclinic bifurcation: from SS back to itself at $\mu = 0.16752429$. (e) At the HK-heteroclinic bifurcation: from SS to the image of SS under l or m' at $\mu = 0.16834331$. (f) At the AHK-homoclinic bifurcation: from SS back to itself at $\mu = 0.16935505$.

and $\sigma = 0.5$ at $\mu = 0.163875$ (see Figure 3b): at the trivial fixed point, $\delta_\sigma = 0.7728$ and if we choose $\zeta = 0.2$ then $\delta_\zeta = 0.3051$; at SS, $\delta_1 = 1.701$ (complex) and $\delta_2 = 0.1701$. We set the global parameters to $E = 0$ (since with $\delta_1 > 1 > \delta_2$, for small z we can drop the $E|z|^{\delta_1}$ term). The parameter F is chosen to be 0.1, which approximately fits the chaotic data in Figure 15(c) – note that this is the only parameter that is fitted to the data as all the eigenvalue ratios are determined analytically. Details of the fitting will be given below. With $Q = 1.0$ (corresponding to Figure 15), the parameter values fall in region I. We illustrate the map (6.12) for these eigenvalue ratios and various values of κ (equivalent to μ) in Figure 18, showing how the map has the same progression from OTC to HK orbits as in the model ODEs (Figure 15). The map and ODE bifurcations are summarised in Figure 16.

The full sequence of bifurcations that leads from OTC to HK orbits involves many local (saddle-node and symmetry-breaking) bifurcations and six principal global (homoclinic and heteroclinic) bifurcations: the connections corresponding to the global bifurcations are shown in Figure 19. With parameters in region I, these bifurcations can be divided into three groups: the gluing bifurcation from OTC to PW, a pair of global bifurcations that bound the interval of chaos in which PW are replaced by PW′, and three global bifurcations involved in the transition from PW′ to HK orbits via an interval of PW4 orbits.

6.5.1. First group: from OTC to PW. At the gluing bifurcation, Γ_+ returns to the SS fixed point (see Figure 19a) in the w direction since $\delta_2 < \delta_1$, so the gluing bifurcation is in the figure-of-eight configuration: both the outgoing and incoming parts of the homoclinic connections are reversed under the action of the reflection symmetry m. Such gluing bifurcations involve stable orbits when the eigenvalue ratio (δ_2 in this case) is greater than one, and unstable orbits when it is less than one.

Glendinning (1989) has shown by combinatorial arguments that if there is a gluing bifurcation in the figure-of-eight configuration that has the net effect of a gluing bifurcation involving stable orbits, but actually involves unstable orbits as the relevant eigenvalue ratio is less than one, then there is a hierarchy of possible bifurcation diagrams connecting the two branches of stable orbits. Glendinning's results need to be reinterpreted in this case, as the global connections can be homoclinic (Figure 19a) or heteroclinic (e). The two simplest examples of Glendinning's hierarchy occur in Figure 16: the simplest, called type (a), is the OTC to PW sequence, involving a pair of saddle-node bifurcations on either side of the gluing bifurcation, with a parameter interval in which stable unglued and stable glued orbits coexist. Type (b), the next simplest, is exemplified by the PW' to HK transition (see below).

With parameters in region I, there is a single transition from OTC to PW; in region II, there is a infinite number of transitions from OTC to PW and back again as orbits accumulate twists near the origin. The additional global bifurcations are created when the line of heteroclinic bifurcations crosses, with increasing Q, from region I into region II. Examples of some of these bifurcations will be given below.

6.5.2. Second group: from PW to PW'. The transition from PW to PW' involves an interval of chaotic trajectories, occurring between the APW-heteroclinic and the PW-heteroclinic bifurcations (Figure 19b and c). In this regime, with κ and Ψ_{11} small, the expression for z is dominated by the $|\Psi_{11}|^{\delta_\zeta}$ term since $\delta_\zeta < \delta_\sigma$, so $z \approx -Q|\Psi_{11}|^{\delta_\zeta}$, and the map T is approximately

$$T(\Psi_{11}, \Psi_{01} = \pm 1) \approx \left(\mathrm{sgn}(\Psi_{11})\left(-\kappa - FQ^{1+\delta_2}|\Psi_{11}|^{\delta_\zeta(1+\delta_2)}\right), -\Psi_{01}\right). \tag{6.16}$$

In this simplified map, the shear changes sign at each iteration, as indeed it does in the ODEs in Figure 15(c) and in the PDEs in Figure 17(c). The behaviour will depend on the magnitude of $\delta_\zeta(1+\delta_2) \approx 0.42$. Since this value is less than one, the interval of chaos and the same sequence of bifurcations as in the Lorenz map (5.14) is expected.

The chaotic behaviour in the ODEs is well described by this map (Figure 20a), but the PDEs are show more complicated behaviour (b), which is not fitted by the map (6.16). This serves as a reminder of the circumstances under which we should expect ODE models to reproduce the dynamics of PDEs near global bifurcations: the connections between equilibria must be the same, and the type (real or complex) and the ordering of the leading (or possibly more) eigenvalues must be the same. In this case, the leading stable eigenvalue of SS (λ_2^-) in the PDEs is complex (rather than real as in the ODEs); we would need to derive a map that allowed twisting at the origin and at the SS fixed points in order to explain this behaviour. Nonetheless, in the other global bifurcations, this complex eigenvalue does not affect the dynamics of the PDEs qualitatively, and the range of r over which there is disagreement is of the order of 10^{-7}. The discrepancy between the ODEs and PDEs is discussed in greater detail below.
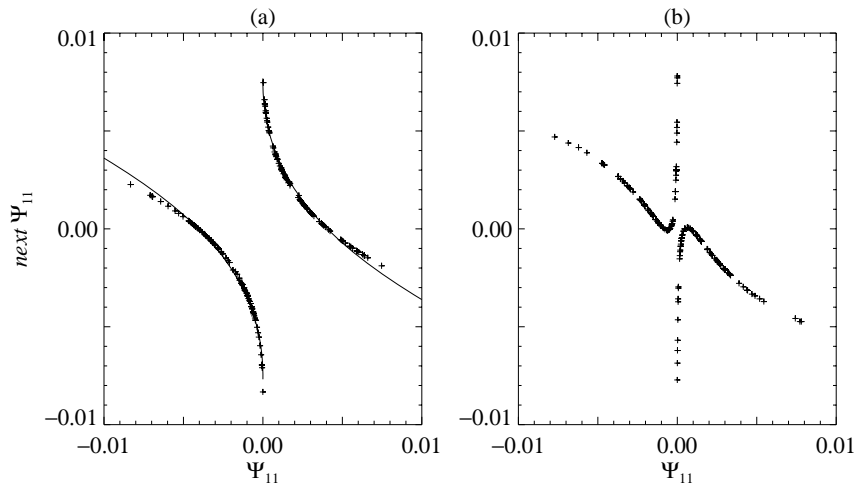
Figure 20. Fitting the map (6.16) to the chaotic oscillations in (a) the ODEs (Figure 15c) and (b) the PDEs (Figure 17c). The crosses represent the values of Ψ_{11} as trajectories cross the plane Σ_0 ($|\Psi_{01}| = 0.02$) plotted against the value at the previous crossing. The solid line is the fitted map. The exponents $\delta_\zeta(1+\delta_2)$ are (a) 0.4204 and (b) 0.4113; the fitted parameters are (a) $\kappa = -0.0079$ and $F = 0.079$. The map (6.16) does not fit the data in the PDEs as the leading stable eigenvalues at SS are complex.

For eigenvalue ratios $\delta_\zeta(1+\delta_2)$ greater than one, there would not be an interval of chaotic trajectories, but instead a transition from (a pair of) PW to (a pair of) PW' orbits, involving an exchange of symmetry, rather than a gain of symmetry as in a normal gluing bifurcation. We have not searched for a heteroclinic bifurcation with eigenvalue ratio greater than one in the ODEs, but conjecture what would happen in this case. Four heteroclinic connections of the type illustrated in Figure 19(c) would be involved in the transition. Just before the heteroclinic bifurcation, the two PW orbits are each made up of a pair of these connections (related to each other by the symmetry m), along with two structurally stable connections from the trivial solution to the SS fixed points. Just after the heteroclinic bifurcation, the two PW' orbits are each made up of a different pair of connections (related to each other by the symmetry m'), along with two structurally stable connections from the trivial solution to the two opposite SS fixed points. One might think that it would be possible to obtain HK orbits from this bifurcation with parameters in region I, but it is not because as the heteroclinic bifurcation is approached, from either side, the shear Ψ_{01} must change sign in the neighbourhood of the origin. If, on the other hand, the shear does not change sign (as in, for example, region III or with $Q = 0$), it is HK and OTC orbits that are involved in the heteroclinic bifurcation.

6.5.3. Third group: from PW' to HK. The transition from PW' to HK orbits involves three global bifurcations (Figure 19d, e and f), and is a type (b) gluing bifurcation (Glendinning 1989). Initially there is a pair of stable PW' orbits (Figure 21a). Only one of the two PW' orbits, which are fixed points of the iterated map $f^2(\Psi_{11})$, is shown. Two PW4 orbits (b) are created in a saddle-node bifurcation. The stable PW4 orbits persist, but the unstable orbits each collide with one of the two SS fixed
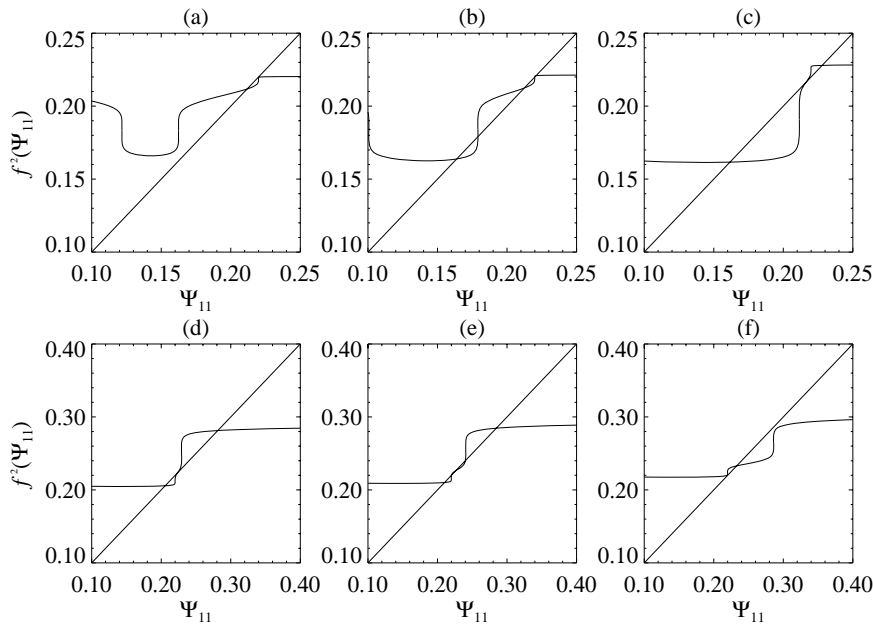
Figure 21. Parameter values as for Figure 18, but with f^2 plotted against Ψ_{11}; (a) $\kappa = 0.183$: the single fixed point is a PW$'$ orbit; (b) $\kappa = 0.184$: a pair of PW4 orbits are created in a saddle-node bifurcation; (c) $\kappa = 0.191$: the PW$'$ orbit loses stability in a subcritical symmetry-breaking bifurcation; (d) $\kappa = 0.250$: the unstable PW$'$ orbit is replaced by an HK orbit after a global bifurcation; (e) $\kappa = 0.255$: the HK orbit gains stability in a subcritical symmetry-breaking bifurcation; and (f) $\kappa = 0.265$: the PW4 orbits are destroyed in a saddle-node bifurcation, leaving a single fixed point representing the HK orbit. Note that in (a) and (f), the graphs of f^2 are almost tangent to the diagonal, but in fact only intersect the diagonal in one place.

points and unglue to form a pair of unstable asymmetric PW$'$ (APW$'$) orbits. Each pair of APW$'$ orbits ends up in a subcritical symmetry-breaking bifurcation (c), where the two PW$'$ orbits lose stability. The unstable PW$'$ orbits collide simultaneously with the two SS fixed points to be replaced with (d) a pair of unstable HK orbits. These gain stability in (e) a subcritical symmetry-breaking bifurcation. Each of the two pairs of asymmetric HK (AHK) orbits collides with an SS fixed point to glue together in pairs to form two unstable PW4 orbits, which are destroyed in a pair of saddle-node bifurcations with the stable PW4 orbits (f).

For larger values of the parameter F, the transition from PW$'$ to HK is through a type (a) bifurcation sequence; this sequence is observed in the PDEs (Figure 17e,f). An additional possibility, which we have discovered only in the map, is that there may be intervals of chaotic behaviour if trajectories approach the trivial solution. Alternatively, if the eigenvalue ratio δ_2 is greater than one, then two stable PW$'$ orbits can be converted to a pair of stable HK orbits when they collide with the two SS fixed points.

Two of the these three global bifurcations in the type (b) sequence just described involve an increase in symmetry: two asymmetric orbits glue together to form a larger symmetric orbit. The APW$'$- and AHK-heteroclinic bifurcations (Figure 19d and f)

are straight-forward gluing bifurcations involving a single SS fixed point, and each forms a PW4 orbit – but not the same one; they are different as the orbits cross the Ψ_{11}-axis with Ψ_{11} negative in Figure 19(d) and positive in (f). Thus a PW4 orbit that is created in a gluing bifurcation when a pair of APW$'$ orbits collides with an SS fixed point is destroyed in an ungluing bifurcation when it collides with the other SS fixed point, forming a pair of AHK orbits.

The other of these three global bifurcations (Figure 19e) involves a change, rather than an increase, in symmetry: PW$'$ orbits (invariant under $t_{m'}$) are replaced by HK orbits (invariant under t_l). This is because the heteroclinic connections are between the SS fixed points, which are mapped to each other by m' or l. The four heteroclinic connections between the two SS fixed points can be fitted together to form periodic orbits in two distinct ways. Thus gluing bifurcations, which involve homoclinic connections, create orbits with increased symmetry, while heteroclinic bifurcations can give an increase in symmetry (OTC going to HK orbits), or a change of symmetry (PW to PW$'$ and PW$'$ to HK orbits) in the case when the heteroclinic connections are between fixed points with the same symmetry type. There is a need for a systematic study of homoclinic and heteroclinic bifurcations in systems with symmetry.

6.6. Unfolding the magnetic map and ODEs

This complicated sequence of local and global bifurcations in the ODEs (3.9) with $Q = 1$ (Figure 16) has the same net effect as the simple heteroclinic bifurcation that converts OTC to HK orbits with $Q = 0$. We have followed the location of the bifurcations in the ODEs using AUTO and the code of Champneys & Kuznetsov (1994); the results in Figure 22(a) show how the whole gamut of bifurcations comes down in a cusp to a single bifurcation at $Q = 0$. Calculating the locations of the global bifurcations in the map (Figure 22b and Table 4) confirms the pattern of bifurcations and the correctness of the approximations made in deriving the map.

The locations of the local and global bifurcations in the ODEs were followed to larger values of Q (Figure 23). The first group of bifurcation lines (the OTC- and PW-saddle-node bifurcations and the OTC-homoclinic, or gluing, bifurcation) all get tied up with the Takens–Bogdanov point, labelled C in the figure. This codimension-two bifurcation point occurs when lines of pitchfork (from SS to STC) and Hopf (from SS to PW) bifurcations coincide, and organises the two routes from SS to PW (Matthews et al 1993). The OTC-saddle-node is created when the Hopf bifurcation from STC to OTC changes from being subcritical to being supercritical.

The remaining global bifurcations (with one exception) continue to larger Q, entering parameter region II when $Q > 2.22$. Since it is the eigenvalues of the trivial solution that become complex in region II, only those heteroclinic bifurcations involving that fixed point are affected: the APW- and PW-heteroclinic bifurcations (Figure 19b and c). As these two lines cross into region II, an infinite number of heteroclinic bifurcations is created. We have not attempted to follow these numerically.

The AHK-heteroclinic bifurcation does not continue to large Q, but turns back and returns to $Q = 0$ at $\mu = 0.1983720$ to form the AHK-heteroclinic gluing bifurcation that forms (HK)^2 orbits. This gluing bifurcation is part of the non-magnetic gluing cascade associated with point B in Figure 5(b). The symmetry-breaking from HK to AHK occurs at $\mu = 0.1903528$ with $Q = 0$. The cusp of bifurcations in Figure 22 will be repeated for this (and subsequent) heteroclinic bifurcations with longer and longer periodic orbits.
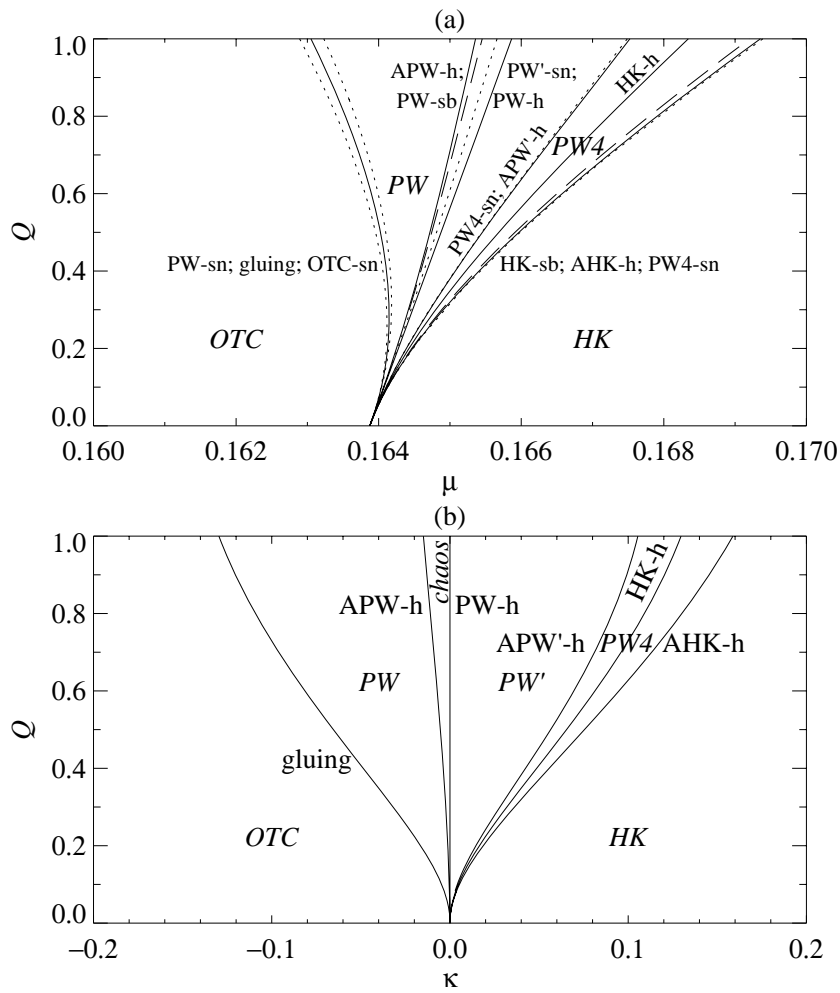
Figure 22. Locations of the local and global bifurcations in (a) the ODEs (3.9) and (b) the map (6.11), with varying Q. The fixed parameters are (a) $\sigma = 0.5$ and $\zeta = 0.2$, and (b) $\delta_\sigma = 0.7728$, $\delta_\zeta = 0.3051$, $\delta_2 = 0.1701$, $E = 0$ and $F = 0.1$. Global bifurcations are shown as solid lines, symmetry-breaking bifurcations as broken lines and saddle-node bifurcations as dotted lines.

These calculations were performed with $\sigma = 0.5$, chosen for the simplest non-magnetic behaviour. With smaller σ, the OTC-heteroclinic gluing bifurcation splits into a wedge of chaotic trajectories with an infinite number of global bifurcations (Figure 10). The map (6.11) could be used to explore the complications that the non-zero magnetic field will introduce in this chaotic regime. On the other hand, with larger σ, the eigenvalue ratio δ_1 (corresponding to the complex stable eigenvalues of SS within the m-invariant subspace) becomes less than one, leading to Shil'nikov chaos; this could be modelled by combining the features of map (5.15) (for complex eigenvalues at SS) with map (6.11) (for non-zero magnetic field and complex eigenvalues at the origin). In fact, in the PDEs, the stable shear eigenvalues (those corresponding to δ_2) are already complex. A map combining all these features would

Table 4. Algebraic conditions satisfied at the global bifurcations in the map (6.12). The global connections are illustrated in Figure 19 and solutions of these equations are in Figure 22(b).

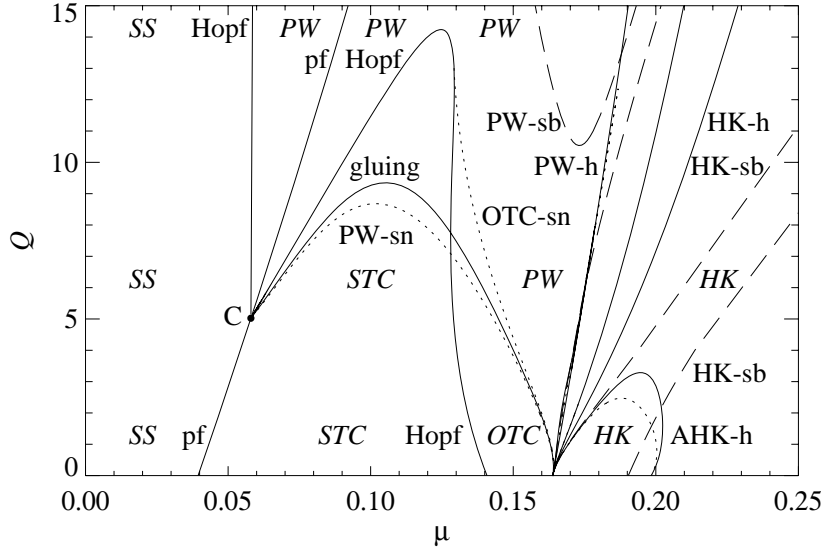| Figure 19	Bifurcation	Defining equation
(a)	OTC-gluing	$z(-\kappa) = 0$ and $\kappa < 0$
(b)	APW-heteroclinic	$f(-\kappa) = 0$
(c)	PW-heteroclinic	$\kappa = 0$
(d)	APW'-heteroclinic	$z(f(-\kappa)) = 0$ and $z(-\kappa) < 0$
(e)	HK-heteroclinic	$z(-\kappa) = 0$ and $\kappa > 0$
(f)	AHK-heteroclinic	$z(f(-\kappa)) = 0$ and $z(-\kappa) > 0$

Figure 23. Locations of the local and global bifurcations in the ODEs (3.9). The fixed parameters are $\sigma = 0.5$ and $\zeta = 0.2$. These parameter values are in region I for $Q < 2.22$ and in region II (complex eigenvalues at the origin) for $Q > 2.22$. The lines have the same meaning as in Figure 22. The lines of OTC-homoclinic (gluing) bifurcations and PW-saddle-node (PW-sn) bifurcations connect to the Takens–Bogdanov bifurcation point (labelled C). Where no attractor is indicated, trajectories are by and large chaotic.

have at the very least trigonometric functions raised to fractional powers, and would have very intricate dynamics.

6.7. Behaviour of the magnetic PDEs

We have already discussed the behaviour of the PDEs with parameters in region I (Figure 17), and noted two discrepancies between the between the behaviour of the PDEs and that of the ODE model. The lack of PW4 orbits in the PDEs we ascribe to their having a different value of the parameter F in the map (6.12). The chaotic interval in the PDEs is not described by a Lorenz map (Figure 20), possibly because of the complex leading stable eigenvalues (corresponding to δ_2) at SS.
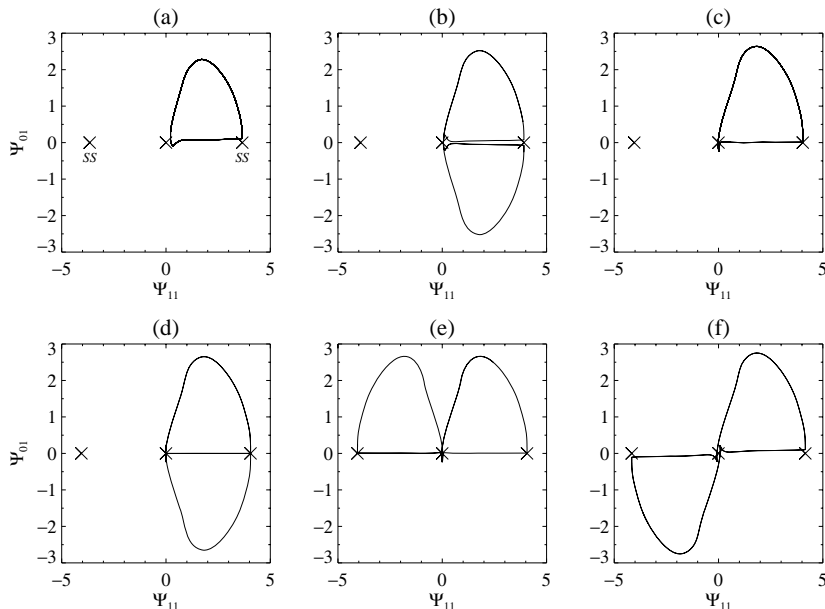
Figure 24. A sequence of global bifurcations in the PDEs, with $Q = 19.74$ ($q = 0.50$), $L = 1.0$, $\sigma = 0.1$ and $\zeta = 0.1$, showing how the orbits wind up around the origin and then unwind. These parameter values are in region II. (a) OTC at $r = 2.000$. (b) After a gluing bifurcation: PW at $r = 2.100$. (c) OTC with a full twist at $r = 2.150$. (d) PW with $1\frac{1}{2}$ twists at $r = 2.156$. (e) HK with a full twist at $r = 2.160$. (f) PW$'$ at $r = 2.200$. At the heteroclinic bifurcation ($r \approx 2.156$), the relevant ratios of eigenvalues are $\delta_r = 0.6940$, $\delta_i = 0.9814$, $\delta_1 = 26.23$ and $\delta_2 = 57.34$ (complex).

Unfortunately, the full story of the behaviour of the PDEs is likely to be even more complicated: since δ_2 corresponds to complex stable eigenvalues and $\delta_2 < 1$, the gluing bifurcation from OTC to PW and that from PW$'$ to HK must follow the symmetric Shil'nikov scenario (Glendinning & Sparrow 1984). In this case, we expect chaotic reversals, with periodic windows of reversing (PW or PW$'$) and non-reversing (OTC and HK) oscillations over a parameter interval around the global bifurcation (Glendinning 1984). We have not observed this behaviour near the gluing bifurcation, only the expected chaotic reversals near the heteroclinic bifurcation in the parameter interval $1.67660185 \le r \le 1.67660190$ (Figure 17c,d). One reason for this may be that the parameter interval of these additional chaotic oscillations is small: not only is δ_2 quite close to one, but the width of the parameter interval will scale with some power of Q as Q becomes small. These additional complications do not change the overall correctness of the picture given by the ODE model and map: the sequence of transitions from OTC to PW to PW$'$ to HK with parameter values in region I.

We have computed solutions of the PDEs for larger Q, wider boxes ($L = 1.0$ or $k = \pi$) and $\sigma = \zeta = 0.1$ (region II) in Figure 24. Trajectories wind up as they approach the heteroclinic bifurcation, going from OTC (a) to PW (b), back to OTC (c), back to PW (d), and so on. After the heteroclinic bifurcation, trajectories unwind, going from HK (e) to PW$'$ (f), the whole picture consistent with Figure 13(b). The sequence is interrupted in this case before the final HK orbit.

7. Discussion

Using ideas from nonlinear dynamics, we have unravelled the complicated shearing behaviour observed in numerical simulations of the PDEs for convection with small Prandtl number σ and in narrow rolls. The low-order sets of ODEs have greatly aided the interpretation of the numerical results, and an understanding of the precise nature of the global bifurcations requires the use of low-dimensional maps.

We have shown under what circumstances pulsating waves, with reversals of shear flow should be expected. With no magnetic field, we find the pitchfork bifurcation to STC occurs when $r \sim 1 + 3\sigma^2 L^2$, with small σ and narrow rolls. This is followed by Hopf and global bifurcations; we do not expect reversals for small Prandtl number σ, and find non-reversing HK oscillations. Since the value of r at which the instability first sets in goes to one as the rolls become narrower and σ goes to zero, the shearing instability is likely to be the first (or at least, one of the first) instability of narrow rolls with small Prandtl number. With moderate Prandtl number (when Ψ_{12} dominates Ψ_{01}), we expect reversing shear (PW′ oscillations) after global bifurcations, and with large Prandtl number, we find a Hopf bifurcation directly to reversing PW oscillations. Understanding the transitions between these regimes as σ is varied remains a challenge.

With a weak magnetic field and narrow rolls, our results indicate PW′ reversals if Ψ_{12} dominates Ψ_{01} and A_{01}, as in the non-magnetic case with moderate σ. With small σ we need $\zeta \leq \sigma$ for PW reversals, or Q large enough for there to be complex eigenvalues at the origin. The PW oscillations are created in a gluing bifurcation and there can be complicated sequences of global bifurcations with increasing r, involving orbits with several different symmetries. The condition $\zeta \leq \sigma$ for reversals of shear can be understood physically in the following way: shear (Ψ_{01}) decays more rapidly than horizontally stretched magnetic field (A_{01}), so when the shear has decayed to small levels and convection is just about to restart, the shear is driven in the opposite direction by the residual magnetic field.

Although the results obtained from our ODE model are strictly valid only in the limit of narrow rolls, we find good qualitative agreement with PDE results for rolls of moderate aspect ratio, $L = 0.5$ (and $L = 1.0$ in Figure 24) for parameter values near global bifurcations. If, however, we select the box size that minimises the critical Rayleigh number, the behaviour is very different. With no magnetic field, we have not found any local bifurcations from SS to STC or PW in the PDEs (for $r \leq 100$ and $0.01 \leq \sigma \leq 100$). For this reason, our results, which relied on perturbing the dynamics near a non-magnetic global bifurcation, will not apply directly. Nonetheless, the presence of a magnetic field encourages narrow rolls (Chandrasekhar 1961), and we have found both the pitchfork to OTC and the Hopf to PW in the PDEs with L set to the value that minimises the critical Rayleigh number. We also find global bifurcations of the type discussed in this paper, and further analysis will be possible.

In the course of analysing this system, we have found novel and interesting nonlinear dynamics in the presence of two reflection symmetries. The symmetries mean that an asymmetric orbit, such as OTC, occurs in four copies that can glue together in a variety of different ways, involving gains of symmetry and subsequent losses or exchanges of symmetry. Our results will be relevant to other systems with the same symmetries and similar mode interactions, such as, for instance, in convection in a horizontal magnetic field (Lantz 1995; Brownjohn *et al* 1995), in models of thermally driven dynamos (Chui & Moffatt 1993), or in the 3D bending instability of rolls in

low-Prandtl-number convection (Massaguer *et al* 1990; Busse *et al* 1992).

This work is the first systematic two-parameter study of the global bifurcations associated with the shearing instability. Our results provide an interpretation of the results of other studies of the magnetic and non-magnetic shearing instability: in narrow rolls, we should expect non-reversing shear with low Prandtl number and reversals with larger Prandtl number. There have been many such studies and their results are all consistent with our findings. In their truncation of the PDEs for 2D Boussinesq convection between stress-free boundaries, Howard & Krishnamurti (1986) found non-reversing chaos with $\sigma = 0.1$ and 1.0 and reversing oscillations, created in a global bifurcation, with $\sigma = 10.0$, all with wavenumber $k = 1.2\pi$, where $k = \pi/L$. Prat *et al* (1995) studied the same PDEs between no-slip boundaries and found a Hopf bifurcation to PW with $\sigma = 10.0$ and $k = 2\pi$. Deardorff & Willis (1965) found reversing oscillations in the same system with $k = \pi$ and $\sigma = 0.71$, though we find a decaying oscillation for these parameter values. Guzdar *et al* (1994) have simulated the experiments of Tabeling *et al* (1990) and found vortices that tilt back and forth (the analogue of our pulsating waves) created in a global bifurcation. Hurlburt *et al* (1984) found vigorous but non-reversing streaming motion in the PDEs for compressible convection between stress-free boundaries with $\sigma = 1.0$ and both $k = 4\pi$ and $k = \frac{2}{3}\pi$. Ginet & Sudan (1987) found unsteady but non-reversing shear in compressible convection using the anelastic approximation, with $\sigma = 1.0$ and $k = 2\pi$. We discuss below how our model can be reinterpreted in the context of compressible convection, where the top and bottom of the layer are no longer equivalent.

There is similar agreement with numerical studies of Boussinesq (described here) and compressible convection in a vertical magnetic field, but Landsberg & Knobloch (1991) and Proctor & Weiss (1993) argued on general grounds that the symmetry-breaking instabilities of SS rolls occur in the compressible case. Weiss (1989) was the first to report PW in the compressible case, with $\sigma = \zeta = 0.1$ and $k = \pi$. This calculation was extended by Proctor *et al* (1994), who investigated the gluing bifurcation in which the PW are created. As discussed in the Introduction, there is no symmetry between the top and bottom of the layer in a stratified atmosphere, and tilted rolls will travel. As a result, it is not possible to fix the phase of the rolls in the box, so there are not just two SS fixed points generated by the discrete translation l, but a whole circle of them, generated by continuous translations. Proctor *et al* (1994) extended our ODE model (3.9) to cover this case by complexifying the Ψ_{11} and Ψ_{12} variables and re-introducing terms that were excluded by the Boussinesq symmetry. Pulsating waves, which now travel back and forth, are created in a symmetry-breaking Hopf bifurcation, and uniformly travelling tilted rolls (travelling waves, or TW), the analogue of STC, are created in a pitchfork bifurcation. As in the Boussinesq case, these two local bifurcations can coincide at a Takens–Bogdanov point with Z_2 symmetry (as in Figure 23), and lines of secondary bifurcations can begin at this point, including Hopf bifurcations from travelling rolls to quasi-periodically modulated rolls (modulated waves, or MW), the analogue of OTC, and then a gluing bifurcation from MW to PW. Thus the global bifurcation in which non-reversing (MW) oscillations are transformed into reversing (PW) oscillations occurs in both the Boussinesq and compressible cases. If this line of global bifurcations is followed away from the Takens–Bogdanov point, the leading eigenvalues of SS may become complex, leading to the possibility of symmetric Shil'nikov dynamics, with chaotic trajectories and periodic windows involving reversing and non-reversing oscillations (Glendinning 1984).

This global bifurcation, and others involving connections between SS fixed points, need to be interpreted carefully in the compressible case. At one of these global bifurcations, the system begins near SS rolls, these rolls tilt over and travel as the shear across the layer is generated, and then the system returns to SS rolls translated from the original rolls. With this interpretation, the homoclinic connections in Figure 19(a) and (e) are not distinguished and are equivalent in the compressible case. Figure 19(d) and (f) represent bifurcations that persist with compressibility as they are associated with changes in the pattern of shear reversals over the course of the oscillation. For example, in the global bifurcation in Figure 19(d) there is a transition from PW′ (shear alternating left and right) to PW4 orbits (shearing twice to the left followed by twice to the right). However, the heteroclinic bifurcations involving the origin will need to be re-examined as these involve transition between orbits that are no longer distinguished on the grounds of symmetry: the OTC and HK orbits in the non-magnetic heteroclinic bifurcation are both MW in the compressible case, and the PW and PW′ orbits (involved in the heteroclinic bifurcations in Figure 19b and c) are equivalent in the compressible case. As a result, it is not clear that these heteroclinic bifurcations, observed in the Boussinesq case with small Prandtl number, will persist once compressibility is introduced.

Three-dimensional convection will obviously generate a much wider variety of solutions than in two dimensions. Physically, an instability to 3D convection should be expected for sufficiently vigorous convection, as magnetic field and shear stretched out in one direction (say, along the x-axis) will suppress x-rolls (with their axis in the y-direction), but will not suppress y-rolls, which act to interchange, but not bend, magnetic field lines (Matthews *et al* 1995). A low-order model can be derived to describe the 3D shearing instability in narrow rolls (Rucklidge & Matthews 1995). The global bifurcations and heteroclinic cycles in the nonmagnetic PDEs and an ODE model are discussed by Matthews *et al* (1996); the magnetic problem will be described in a future paper.

Acknowledgments

References

A Arnéodo, P Coullet and C Tresser 1981 A possible new mechanism for the onset of turbulence *Phys. Lett.* **81A** 197–201

W-J Beyn 1990 The numerical computation of connecting orbits in dynamical systems *IMA J. Num. Anal.* **9** 379–405

D P Brownjohn, N E Hurlburt, M R E Proctor and N O Weiss 1995 Nonlinear compressible magnetoconvection. Part 3. Travelling waves in a horizontal field *J. Fluid Mech.* **300** 287–309

N Brummell and K A Julien 1996 On the shearing instability in Rayleigh–Bénard convection (in preparation)

F H Busse 1983 Generation of mean flows by thermal convection *Physica* **9D** 287–299

F H Busse, M Kropp and M Zaks 1992 Spatio-temporal structures in phase-turbulent convection *Physica* **61D** 94–105

A R Champneys and Yu A Kuznetsov 1994 Numerical detection and continuation of codimension-two homoclinic bifurcations *Int. J. Bifurcation and Chaos* **4** 785–822

S Chandrasekhar 1961 *Hydrodynamic and Hydromagnetic Stability* (Oxford: Clarendon Press)

A Y K Chui and H K Moffatt 1993 A thermally driven disc dynamo *Solar and Planetary Dynamos* ed M R E Proctor, P C Matthews and A M Rucklidge (Cambridge: Cambridge University Press) pp 51–58

J D Crawford and E Knobloch 1991 Symmetry and symmetry-breaking bifurcations in fluid dynamics *Annu. Rev. Fluid Mech.* **23** 341–387

J W Deardorff and G E Willis 1965 The effect of two-dimensionality on the suppression of thermal turbulence *J. Fluid Mech.* **23** 337–353

M Dellnitz and C Heinrich 1995 Admissible symmetry increasing bifurcations *Nonlinearity* **8** 1039–1066

E Doedel and J Kernévez 1986 *AUTO: Software for Continuation and Bifurcation Problems in Ordinary Differential Equations* (Pasadena: CalTech Press)

J F Drake, J M Finn, P Guzdar, V Shapiro, V Shevchenko, F Waelbroeck, A B Hassam, C S Liu and R Sagdeev 1992 Peeling of convection cells and the generation of sheared flow *Phys. Fluids B* **4** 488–491

G P Ginet and R N Sudan 1987 Numerical observations of dynamic behavior in two-dimensional compressible convection *Phys. Fluids* **30** 1667–1677

P Glendinning 1984 Bifurcations near homoclinic orbits with symmetry *Phys. Lett.* **103A** 163–166

P Glendinning 1985 Homoclinic bifurcations *PhD dissertation* Cambridge

P Glendinning 1988 Global bifurcations in flows *New Directions in Dynamical Systems* ed T Bedford and J Swift (Cambridge: Cambridge University Press) pp 120–149

P Glendinning 1989 Global structure of homoclinic bifurcations: a combinatorial approach *Phys. Lett.* **141A** 391–396

P Glendinning and C Sparrow 1984 Local and global behaviour near homoclinic orbits *J. Stat. Phys.* **35** 645–696

M Golubitsky, I Stewart and D G Schaeffer 1988 *Singularities and Groups in Bifurcation Theory. Volume II* (New York: Springer)

J Guckenheimer and P Holmes 1983 *Nonlinear Oscillations, Dynamical Systems and Bifurcations of Vector Fields* (New York: Springer)

P N Guzdar, J M Finn, A V Rogalsky and J F Drake 1994 Two-dimensional nonlinear dynamics of four driven vortices *Phys. Rev.* **49E** 2062–2069

K B Hermiz, P N Guzdar and J M Finn 1995 Improved low-order model for shear flow driven by Rayleigh–Bénard convection *Phys. Rev.* **51E** 325–331

L N Howard and R Krishnamurti 1986 Large-scale flow in turbulent convection: a mathematical model *J. Fluid Mech.* **170** 385–410

D W Hughes and M R E Proctor 1990 A low-order model of the shear instability of convection: chaos and the effect of noise *Nonlinearity* **3** 127–153

N E Hurlburt, J Toomre and J M Massaguer 1984 Two-dimensional compressible convection extending over multiple scale heights *Astrophys. J.* **282** 557–573

E Knobloch, N O Weiss and L N Da Costa 1981 Oscillatory and steady convection in a magnetic field *J. Fluid Mech.* **113** 153–186

R Krishnamurti and L N Howard 1981 Large-scale flow generation in turbulent convection *Proc. Nat. Acad. Sci. U.S.A.* **78** 1981–1985

A S Landsberg and E Knobloch 1991 Direction-reversing traveling waves *Phys. Lett.* **159A** 17–20

S R Lantz 1995 Magnetoconvection dynamics in a stratified layer. II. A low-order model of the tilting instability *Astrophys. J.* **441** 925–941

E N Lorenz 1963 Deterministic nonperiodic flow *J. Atmos. Sci.* **20** 130–141

G D Lythe 1995 Dynamics controlled by additive noise *Nuovo Cimento* **17D** 855–861

D V Lyubimov and M A Zaks 1983 Two mechanisms of the transition to chaos in finite-dimensional models of convection *Physica* **9D** 52–64

J M Massaguer, I Mercader and M Net 1990 Nonlinear dynamics of vertical vorticity in low-Prandtl-number thermal convection *J. Fluid Mech.* **214** 579–597

P C Matthews, N E Hurlburt, M R E Proctor and D P Brownjohn 1992 Compressible magneto-convection in oblique fields: linearized theory and simple nonlinear models *J. Fluid Mech.* **240** 559–569

P C Matthews, M R E Proctor, A M Rucklidge and N O Weiss 1993 Pulsating waves in nonlinear magnetoconvection *Phys. Lett.* **183A** 69–75

P C Matthews, M R E Proctor and N O Weiss 1995 Compressible magnetoconvection in three dimensions: planforms and nonlinear behaviour *J. Fluid Mech.* **305** 281–305

P C Matthews, A M Rucklidge, N O Weiss and M R E Proctor 1996 The three-dimensional development of the shearing instability of convection *Phys. Fluids* **8**

D R Moore and N O Weiss 1973 Two-dimensional Rayleigh–Bénard convection *J. Fluid Mech.* **58** 289–312

J Prat, J M Massaguer and I Mercader 1995 Large-scale flows and resonances in 2-D thermal convection *Phys. Fluids* **7** 121–134

M R E Proctor and D W Hughes 1991 The false Hopf bifurcation and noise sensitivity in bifurcations with symmetry *Eur. J. Mech. B* **10** 81–86

M R E Proctor and N O Weiss 1990 Normal forms and chaos in thermosolutal convection *Nonlinearity* **3** 619–637

M R E Proctor and N O Weiss 1993 Symmetries of time-dependent magnetoconvection *Geophys. Astrophys. Fluid Dynamics* **70** 137–160

M R E Proctor, N O Weiss, D P Brownjohn and N E Hurlburt 1994 Nonlinear compressible magneto-convection. Part 2. Streaming instabilities in two dimensions *J. Fluid Mech.* **280** 227–253

A M Rucklidge 1992 Chaos in models of double convection *J. Fluid Mech.* **237** 209–229

A M Rucklidge 1993 Chaos in a low-order model of magnetoconvection *Physica* **62D** 323–337

A M Rucklidge 1994 Chaos in magnetoconvection *Nonlinearity* **7** 1565–1591

A M Rucklidge 1996 Symmetry-breaking instabilities of convection in squares *Proc. R. Soc. Lond. A* (submitted)

A M Rucklidge and P C Matthews 1993 Shearing instabilities in magnetoconvection *Solar and Planetary Dynamos* ed M R E Proctor, P C Matthews and A M Rucklidge (Cambridge: Cambridge University Press) pp 257–264

A M Rucklidge and P C Matthews 1995 The shearing instability in magnetoconvection *Double-Diffusive Convection* ed A Brandt and H J S Fernando (Washington: American Geophysical Union) pp 171–184

G Rüdiger 1989 *Differential Rotation and Stellar Convection: Sun and Solar-type Stars* (Berlin: Akademie-Verlag)

A L Shil'nikov 1986 Bifurcations and chaos in the Morioka–Shimizu system (in Russian) *Methods of Qualitative Theory of Differential Equations* Gorky State University, 180–193. Published in English (1991) *Selecta Math. Sov.* **10** 105–117

E D Siggia 1994 High Rayleigh number convection *Annu. Rev. Fluid Mech.* **26** 137–168

C Sparrow 1982 *The Lorenz Equations: Bifurcations, Chaos, and Strange Attractors* (New York: Springer)

P Tabeling, O Cardoso and B Perrin 1990 Chaos in a linear array of vortices *J. Fluid Mech.* **213** 511–530

R Thompson 1970 Venus's general circulation is a merry-go-round *J. Atmos. Sci.* **27** 1107–1116

N O Weiss 1989 Time dependent compressible convection *Solar and Stellar Granulation* ed R J Rutten and G Severino (Dordrecht: Kluwer) pp 471–480

G E Willis and J W Deardorff 1970 The oscillatory motions of Rayleigh convection *J. Fluid Mech.* **44** 661–672